The topology of gas jets injected beneath a surface and subject to liquid cross-flow

Journal:	*Journal of Fluid Mechanics*
Manuscript ID	JFM-16-S-0365.R3
mss type:	Standard
Date Submitted by the Author:	n/a
Complete List of Authors:	Mäkiharju, Simo; UC Berkeley, Mechanical Engineering Lee, In-Ho; University of Michigan, Department of Naval Architecture and Marine Engineering Filip, Grzegorz ; University of Michigan, Department of Naval Architecture and Marine Engineering Maki, Kevin; University of Michigan, Department of Naval Architecture and Marine Engineering Ceccio, Steven; University of Michigan, Department of Naval Architecture and Marine Engineering
Keyword:	Gas/liquid flows < Multiphase and Particle-laden Flows, Jets < Wakes/Jets

Under consideration for publication in J. Fluid Mech.

The topology of gas jets injected beneath a surface and subject to liquid cross-flow

Simo A. Mäkiharju[1,+], In-Ho R. Lee[2], Grzegorz P. Filip[2], Kevin J. Maki[2], and Steven L. Ceccio[2]

[1]Department of Mechanical Engineering, University of California, Berkeley, California 94720, USA
[2]Department of Naval Architecture and Marine Engineering, University of Michigan, Ann Arbor, Michigan 48109, USA

Gas injection into a liquid cross-flow is examined for the case where the gas is injected beneath a horizontal flat surface. For moderate Froude numbers, the gas pocket that is formed will rise toward the flow boundary under the action of buoyancy, a condition that is conducive to the formation of gas layers for friction-drag reduction on the surface. At the location of gas injection, a plume whose geometry is related to the mass and momentum flux of the injected gas and liquid cross-flow is formed, and the influence of buoyancy is minimal. However, as the gas pocket convects downstream, buoyancy brings the gas back upward to the flow boundary, and leads to the bifurcation of the pocket into two distinct branches, forming a stable "V"-shape. Under some conditions, the flow between the two gas branches is almost entirely liquid, while for others there exists a bubbly flow or a continuous sheet of gas between the branches. The sweep angle and cross-sectional geometry of the gas branches are related to free-stream speed and boundary-layer thickness of the liquid cross-flow, the mass-injection rate of the gas, the diameter of the injection orifice, and the gas outlet mean velocity and gas-jet angle. Data for a range of experimental conditions are used to scale the flow and results are compared to numerical computations of the flow, and these data are used to illustrate the underlying flow processes responsible leading to the formation the stable and straight gas branches. A simple model based on the balance of forces around a stable gas branch is presented and used to scale the observed data, and we use the results of this analysis and the computations to discuss how the process of gas injection may interact with the formation of the stable gas pockets farther downstream.

1. Introduction

The interaction of a jet in a cross-flow has received considerable attention, especially for the case when the jet and free-stream flows consist of fluids with the same or similar density and compressibility, and a recent review of this topic has been provided by Mahesh (2013). In the present study, we examine a particular flow that has received considerably less attention: the injection of a gas into a liquid cross-stream. Given the large difference between the density of the gas and liquid, the mechanisms for mass and momentum transport between the gas and the liquid may also differ considerably from flow with similar material phase with buoyancy playing an important factor. The motivation for this effort arose from the desire to create gas layers beneath the hulls of

[*]E-mail address for correspondence: makiharju@berkeley.edu

marine vehicles to reduce the skin friction (Ceccio, 2010), and thus improve the vehicles' energy economics (Mäkiharju *et al.* 2012). Air layer drag reduction (ALDR) has been successfully achieved by injection of gas beneath a hull *via* a slot injector (Sanders *et al.* 2006, Elbing *et al.* 2008, Elbing *et al.* 2013). For the practical application of ALDR, it may be advantageous in terms of the hull mechanical structure and the marine engineering of the gas delivery to inject the gas from discrete orifices in the hull, rather than *via* a long slot. To that end, this study was conducted to examine how gas is distributed beneath a flat surface after it is injected from an orifice into a liquid cross-flow.

Despite the canonical nature of this flow, few studies have been published regarding the injection of gas into a liquid cross-flow for cases where a gas pocket is formed at the injection location, rather than the immediate formation of bubbles at the injection orifice as discussed by Wace *et al.* (1987). Pignoux (1998) investigated a horizontal gas jet injected into a vertical liquid cross-flow, where the direction of gravity is aligned with the mean liquid flow direction. The injected gas jet was deflected by the incoming liquid flow and formed a distinct gas pocket, with a shape that is reminiscent of a Rankine half-body formed by a source in a cross-flow, but having an ellipsoidal shape. The high void fraction gas pocket then transitioned into a multiphase recirculating region, which subsequently broke down into a bubbly flow that convected downstream from the cavity closure. Pignoux (1998) also measured the spatial evolution of the void fraction in the gas pocket and the resulting bubbly wake. Vigneau *et al.* (2001a) examined how changes in the upstream liquid boundary layer influence the topology of the gas pocket, showing little effect. And, Vigneau *et al.* (2001b) examined the interaction of multiple gas jets emitted from several orifices. Insel *et al.* (2010) reported on air injection through circular orifices beneath a model-scale ship hull, a flow that is closest to that of interest in the present study. Their observations revealed that the gas flow from a single injection port splits into two branches, described as "V"-shape. The gas spreading angles between two branches were measured and analyzed for different cross-flow speeds and air injection rates, and they also examined injection through multiple injection ports. However, no general scaling for the spreading angle (or topology in general) as a function of flow conditions has been formulated.

Figure 1 presents a schematic diagram of the basic cavity topology for gas injection into liquid cross-flow, when gravity is oriented such that buoyancy brings the gas toward the flat flow boundary, and hence buoyancy may play an important role in the evolution of the gas-pocket topology. Figure 2 presents typical images of the gas pocket. Near the gas injection port, we see the formation of a gas pocket that is similar to those observed by Pignoux (1998), where buoyancy acts parallel to the free-stream (and therefore has a much reduced influence on the cavity dynamics). However, as the gas beneath the surface convects downstream, we observe a two-branched pattern similar to that reported by Insel *et al.* (2010), except in the present study two distinct topological variations of the V-shaped cavity are observed; one where the region between the branches contains practically no air (*i.e.* a Lambda, Λ, type cavity) and one where the region is covered by a continuous air layer (*i.e.* Delta, Δ, type cavity).

We should also note the similarity in appearance to other bifurcating jets (where jet and fluid are both either liquid or gas) forming as the jet divides into separate vortex streams in absence of surfaces (Reynolds *et al.* 2003), as the buoyant jet encounters a free

surface (Abdelwahed & Chu, 1978), or as the jet impinges on a solid surface (Choi *et al.* 2015). While bifurcation in the former is not thought to be due to the same mechanism as that causing the bifurcation in the present study, it is less clear if the bifurcation mechanism in the latter two cases is analogous to the present flow under consideration here.

In the present study, we examine gas pockets as they are formed *via* gas injection from a single orifice into a liquid cross-flow. We combine experimental observations with computations to study the basic flow processes responsible for the formation of the V-shaped gas pocket, and attempt to show how the flow parameter such as the free-stream speed, boundary layer profile, gas mass injection rate, size of the orifice and gas injection angle change the topology of the gas pocket. The organization this paper is as follows: in Section 2 we introduce the experimental setup, in Section 3 we discuss the numerical model, Section 4 discusses the cavity topology, Section 5 discusses how the computed results explain the topology and Section 6 presents a simplified scaling of the gas-pocket topology.

2. Experimental Setup

The experiments were performed in the Physical Modeling Basin of the Marine Hydrodynamic Laboratory at the University of Michigan. The basin has 109.7 m carriage running length with 6.7 m width and 3.2 m depth. A manned carriage transports instruments and a towed model along the basin at speeds ranging from $0.1 \leq U_\infty \leq 6.1$ ms^{-1}. During testing, up to a 30 minute interval was taken between every run to ensure a calm water condition for the subsequent run. The water level was adjusted daily such that it was constant for all experiments.

Two barge models with flat bottoms, and producing nominally two-dimensional inflow boundary layers, were utilized. Gas-injections tubes with their ends flush with the flow boundary were inserted through the bottom of the barges in vertical orientation. The flow rate of the injected air, Q_i, and free-stream speed U_∞ were independently varied. Image-based measurements were recorded around the gas injection location using an imager viewing the gas pocket from below. A more detailed description of the models and setup is presented in Lee (2015).

2.1 *Towed test models*

Two different barge models, Barge I and Barge II, were used as they had different boundary-layer thickness at the location of gas injection. Schematic diagrams of the two test models are shown in figure 3. Both models had a transparent bottom to enable real-time observation of the gas injected underneath. The models were rigidly fixed with four struts to the carriage to prevent any motion relative to the carriage, and had a constant 81 mm draft.

Barge I had overall dimensions of 4.3 m in length, 0.7 m in width, and 0.3 m in height. The span-wise uniform bow had a slope of 8.0°. Particles of 150 μm mean diameter were randomly scattered and affixed across the span of the model 1.0 m from the leading edge of the model on a 0.1 m wide strip to induce turbulent boundary layer transition upstream of the injection location. The resulting boundary layer profile was measured at the model

centerline at the gas injection location 0.4 m downstream of the beginning of the flat bottom.

Barge II had overall dimensions of 6.5 m in length, 1.5 m in width, and 0.3 m in height. In order to reduce air ingestion at higher speeds, the bow was modified and consisted of a submerged flat plate with an elliptic planform fixed to a surface-piercing wedge. Particles of 150 μm mean diameter were randomly scattered and affixed across the span of the model 1.3 m from the leading edge of the model on a 0.2 m wide strip to induce turbulent boundary layer transition ~0.5 m upstream of the injection location.

Unless stated otherwise for a specific figure, the coordinate system is chosen such that the origin is at the center of the injector, *x*-axis points downstream (towards stern) and *y*-axis is normal to the surface parallel to gravity vector (*i.e. y* increases with depth).

2.2 *The boundary layer upstream of gas injection*

The boundary layer profiles for each barge model and flow speed were measured at the location of the air injection by traversing a pitot tube (Omega Engineering PBE-H-M) in the *y*-direction. The pitot was translated from 0 mm (flush with the bottom of the model surface) to 250 mm beneath the surface. The dynamic pressure at each height was measured using a 0-to-17 kPa differential-pressure transducer (Omega Engineering PX409-2.5DWU5V) with manufacturer specified accuracy of ±14 Pa. Boundary-layer profiles for both barge models are presented in figure 4, with δ_1 and δ_2 representing the boundary layer thickness for Barges I and II, respectively. The data suggest that the boundary layers are turbulent at the location of gas injection for all conditions discussed in this paper.

2.3 *The gas injection system*

The gas-injection system was designed to generate, regulate, and measure a stable air mass flow rate. A 1.2 kW air compressor was used to supply a 0.30 m^3 reservoir maintained at 650 kPa. Airflow from the pressure reservoir was controlled by a pressure regulator that supplied the flow meters with 101 to 308 kPa air. Multiple Omega Engineering FMA 5400/5500 series gas mass flow controllers were used to maintain accurate measurement of the air mass flow rate over a wide range. The accuracy of the mass flow meters was $\pm$3% of full scale (corresponding to at most $\pm$10% of the reported value). Rotameters (Omega Engineering FL2003 and FL2001) were also used to confirm the measured flow rates with accuracies of $\pm$5% of full scale.

Different gas-injection tubes were used to change both the diameter of the orifice, D_i, and gas jet angle with respect to the free-stream flow, β. Tubes were fabricated with fixed outer diameter, and various inner diameters. For Barge I, the orifice diameters were 6.0 and 10.0 mm, and for Barge II, they were 4.9, 10.2, and 19.7 mm. For simplicity, we will denote the diameters with the nominal values of D_i = 5 mm, 10 mm, and 20 mm. To enable the assumption of a fully developed pipe flow, the pipes had a straight lead-up section of at least 20 D_i before the exit. Three-dimensional printing was used to fabricate angled injection tubes. For angled injectors, only the data from 5 mm inner diameter tubes are included. The injection angle, β, was defined with respect to the bottom surface of the barge (see figure 1), and the injection angle varied from $22.5° \leq \beta \leq 157.5°$. To

calculate the average injected gas velocity, $\underline{U_i}$, the measured mass flow rate of the air was converted to a volume flow rate at the static pressure at the fixed barge draft (81 mm).

2.4 *Video imaging systems*

A stationary high-speed cinematography system (Phantom v710 camera in a custom watertight enclosure) was installed at the bottom of the basin, 3 m beneath the free surface to view the bottom of the model as it passed over at mid tank 49 m from the starting point of the carriage. Ten 100 W (8500 lm) LED lights were used to illuminate the barge as it passed through the camera's field of view. High-speed videos were recorded with 1440 x 1080 pixel resolution at 200 Hz frame rate and 5 ms exposure time.

2.4 *Experimental test conditions*

The independent parameters of the experiment consisted of the free-stream flow speed (*i.e.* the carriage speed), U_∞, boundary layer thickness at the injection location, δ, diameter of the gas injection orifice, D_i, gas injection angle β, and the volume flow rate of the gas (at draft pressure), Q_i. The ranges of these parameters are presented in Table 1. The densities $\rho_i = 1.2$ kgm^{-3} and $\rho_\infty = 1000$ kgm^{-3}, and kinematic viscosities $\nu_i = 1.5 \times 10^{-5}$ m^{2}s^{-1} and $\nu_\infty = 1.0 \times 10^{-6}$ m^{2}s^{-1} of the gas jet and the liquid water cross-flow are assumed to be constant throughout the experiments. The water and air temperatures were 20 ± 1^oC.

3. Numerical Model

The numerical simulations were performed using the open-source finite-volume Computational Fluid Dynamics (CFD) toolkit OpenFOAM 2.3 (www.openfoam.com) that consists of a set of numerical solvers and discretization schemes commonly used to solve partial differential equations that govern fluid flow.

3.1 *Description of the numerical method*

The governing equations are the conservation of mass and momentum equations for an incompressible fluid with varying mechanical properties of density and viscosity. The numerical solver is based on a formulation of the incompressible Navier-Stokes equations for multiphase flow used by Scardovelli & Zaleski (1999). The volume-of-fluid (VOF) method of Hirt & Nichols (1981) is adopted here and surface tension is incorporated through the continuum surface force (CSF) approach of Brackbill *et al.* (1992). In all simulations, the surface tension coefficient is taken as $S = 0.07$ Nm^{-1}. The gas-liquid interface is defined as the contour of 50% void fraction within the computational domain.

The discretized equations are solved on unstructured grids composed of hexahedra and prism elements. The spatial terms of the governing equations are discretized based on the generalized Gauss' theorem and a combination of second-order linear and linear-upwind schemes. The temporal terms are handled implicitly using the second-order backwards Euler scheme. The flow quantities are stored at the cell centers in a co-located arrangements and the system of equations is solved in a segregated manner through the PISO (Pressure Implicit with Splitting of Operators) algorithm.

3.2 *Boundary conditions*

The rectangular computational domain has overall dimensions of 1.20 m in length, 1.00 m in width, and 0.20 m in height. The air injector is located at the origin that is on the centerline and 0.20 m downstream from the upstream inlet boundary. The cylindrical injector has a diameter of 10 mm and it is modeled with a no-slip wall that extends 0.02 m above the no-slip flat bottom of the barge. The air injection rate is prescribed at the injector boundary and the water upstream inlet boundary is assigned the mean boundary layer profiles measured in the physical experiments. The downstream outlet boundary is prescribed a fixed pressure value and the lateral and bottom boundaries are modeled as slip walls. See figure 5 for a depiction the flow domain on the center plane and on the wall near the injector. The reported pressure is calculated relative to the value at the outlet boundary, which produces positive and negative values.

3.3 *Grid resolution and solution convergence*

The spatial and temporal discretization is selected based on a grid convergence study. The solution for $U_\infty = 3.0$ ms^{-1}, $Q_i = 2.5 \times 10^{-3}$ m^{3}s^{-1}, $\delta = 51$ mm, $D_i \sim 10$ mm, and $\beta = 90^o$ (Case A) is computed on a set of three geometrically similar grids. Each grid is uniform in the region where the air-water interface passes. Details of the grids are summarized in Table 2. A time-step size of 1.3×10^{-6} s is used to ensure that the maximum Courant number remains below 1 for all simulations. All simulations completed were performed on the Stampede cluster that is a part of the XSEDE network (Towns *et al.*, 2014). The time-averaged air-cavity profiles obtained using the three grids are compared in figure 5. The time-averaging is performed over a time window of 1 second, after 1 second of simulation time has passed. In dimensionless time, $t^* = tU_\infty/D_i$, the shortest averaging window was $t^* = 200$. The lowest oscillation frequency in the flow is approximately $t^* \sim 5$, and hence the shortest averaging window contained a minimum of 40 oscillations. All three grids show a strong agreement especially in the proximity of the injector and near the reattachment region. The fine grid is used for all of the simulations and analysis presented in this paper.

4. The Cavity Topology

When the gas jet discharges from the injection hole with diameter D_i into the cross-flow, the diameter of the jet increases to D_E, and the gas forms a single pocket near the injector. The gas jet is deflected by the oncoming liquid flow, but it often undergoes a "puffing" behavior where the volume flux varies around a mean level with some fixed frequency. Farther downstream from the injection location, the gas pocket reaches a maximum thickness and begins to close on the model surface. As the gas pocket closes at the centerline, it cleaves into two distinct pockets of gas ("branches"). In many cases, the majority of the injected gas flows into the two branches, while in others some gas fills the region between the branches more or less continuously. Topologies of the resulting flow are broadly classified into three different types: Delta type (Δ) that have a bubbly flow or thin air layer between the branches, Lambda type (Λ) that have little to no interstitial air, and Transition type (T) which has air partially covering the region in between branches.

Figure 6 presents stitched image (combining multiple images recorded as the barge passes over the stationary camera) of the larger gas pocket topologies for both Delta type and Lambda type.

As the flow develops along the surface, the gas branches were stable until they either impinge on the edges of the barge model or broke down after loss of gas as a result of entrainment in the branch cavity closure. Three quantities (shown in figure 1b) were derived from images of the gas cavity: the sweep angle of the branches φ, the chord length of the branch C, and the equivalent diameter of the jet, D_E. The sweep angle of the branch was measured from the plane perpendicular to the cross-flow direction to the edge of the branch. The reported chord length was based on the measurement of average branch thickness of a ~0.25m long section of the branch, measured at the thickest part off the branch. The procedure was discussed in detail by Lee (2015), where the uncertainty of the chord length measurement was estimated to be ±5mm. We should also note that in some instances the chord shrunk notably downstream due gas loss from the branch, and potentially due to other yet to be well characterized factors.

4.1 *The gas pocket formed near at the location of gas injection*

The flow near the location of gas injection resembles that reported by Pignoux (1998), Vigneau *et al.* (2001a), and Vigneau *et al.* (2001b) for the injection of gas into a downward flowing vertical stream. They reported that the gas injected from the circular orifice on the surface of a flat wall (*i.e*. the wall of the test section) would form a gas pocket for a range of free-stream velocity, boundary-layer thickness, and mass-flux of gas. The shape of the gas pocket was analogous to that of a Rankine half-body, but with a nominal shape of a semi-ellipsoid. The axis of the ellipsoid in the wall normal direction of the injected gas was typically larger than the axis in the cross-stream direction. The gas pocket, once formed, would grow in cross-sectional area with downstream distance until a critical cross-sectional area was reached. Then, the cavity would break down into a recirculating bubbly mixture, with bubbles being continually entrained in the cavity wake. These investigators measured the cavity gas-liquid interfacial profiles, cavity cross-sectional area, and gas-pocket length for varying liquid flow speed, gas mass flow rate, orifice size, and boundary-layer thickness.

Despite its relative simplicity, this near-injector flow is particularly difficult to scale. It is helpful to draw a comparison to the liquid flow around an axisymmetric cavitator, as discussed by Franc & Michel (2005). Here, a *solid* object placed in the liquid flow leads to the creation of a low-pressure gas-filled cavity in its wake. The dimensions of the cavity are principally related to the drag coefficient and radius of the cavitator, and the cavitation number (*i.e.* the under-pressure of the cavity) defined as $\sigma = (P_\infty - P_C)/\frac{1}{2}\rho U_\infty^2$. The resulting cavity is approximated by an ellipsoid far from the cavitator, and with decreasing cavitation number, the radius and length of the cavity increases. If non-condensable gas is directly injected into the liquid, the *gas itself* serves as the cavitator; therefore, the static pressure of the gas exiting the orifice must exceed the stagnation pressure of the incoming flow. Figure 7 shows the instantaneous cavity profile and time-traces of the normalized pressure at the injector from the CFD, and the gas exit pressure can indeed be seen to exceed the cavity pressure in the boundary layer at jet penetration depth $\overline{p}$, where

$$\bar{p} = P / \frac{1}{2}\rho_\infty U_\infty^2 \quad (4.1)$$

Note that the pressure is calculated relative to the value at the outlet boundary, and hence takes values that are positive and negative. The effective drag and size of the cavitator will depend on the extent to which the gas penetrates the flow for a given mass, velocity, and momentum flux of the injected gas, the injection angle, the free-stream liquid speed, and, to a lesser extent, the thickness of the boundary layer compared to the size of the orifice. The unsteadiness of the cavity exit pressure shown in the figure will also be discussed below.

If the cavity pressure remains below the free-stream pressure, the cavity will reach a maximum cross-section and then close. And, the maximum cross-sectional area of the cavity is proportional to the effective cavitator drag and cavity under-pressure (a consequence of streamwise momentum conservation). If the cavity pressure rises to the static pressure of the flow (*i.e.* cavitation number approaches zero), the cavity will not close (*i.e.* it will be a super-cavity). In the case of injected non-condensable gas, the mean streamwise gas velocity within the cavity will decrease as the cavity expands, and if the average streamwise velocity of the gas reaches the free-stream velocity before the cavity has reached its maximum cross-sectional area, the pocket breaks down into a bubbly mixture. Conversely, if the average gas velocity reaches the free-stream velocity at or after the location of maximum cavity cross sectional area, the gas pocket can persist. Therefore, it is the interaction of the relative gas volume flux and momentum flux of the gas jet that will determine the drag on the liquid at the point of injection, and the downstream position where the cavity might break down into a bubbly mixture. A scaling that captures this complex phenomenon has yet to be presented; however, Vigneau *et al.* (2001a) demonstrated that modest changes to the thickness of the liquid boundary layer did not have a significant influence on the behavior of the gas pocket, and Vigneau *et al.* (2001b) scaled the cross-sectional area of the gas pocket breakdown with the gas volume flux and the free-stream speed.

To illustrate the features of this flow, a computation was performed of gas injection into the liquid for conditions of zero buoyancy (*i.e.* without gravity) for U_∞= 3.0 ms^{-1} and D_i = 10 mm, β = 90.0°, and Q_i = 5 x 10^{-3} m^{3}s^{-1}. Figure 8 shows the time-averaged flow field around the injector in the *x*-*z* and *x*-*y* planes. The location of the cavity interface, static pressure, and flow speed with velocity vectors are presented. The stagnation region around the orifice is clearly visualized, along with the turning of the gas jet by the liquid flow. The flow speed of the gas decreases until it reaches the average free-stream speed, and the cavity reaches a nearly constant cross-sectional area. This is a higher gas volume flux compared to those reported by Vigneau *et al.* (2001b), and thus the gas pocket persists for a longer distance from the injector.

The steady flow described above occurs when there is equilibrium between the static pressure of the gas jet near the orifice and the stagnation pressure of incoming liquid. Pignoux (1998) noted, however, that the gas would not necessarily exit steadily, but would undergo a periodic variation in the flow rate, resulting in a puffing effect. This was also observed in the present study in both experiments (figure 9a and 9b) and CFD (figure 7 and 9c). This phenomenon results from the pinch-off of the orifice by an encroaching liquid flow at the base of the jet. If balance between the liquid stagnation

pressure and the jet static pressure is perturbed, the liquid can move over the orifice, blocking the gas flow, and increasing the gas pressure upstream of the orifice. In turn, the buildup in gas pressure will eventually blow back the liquid, moving the stagnation region upstream of the orifice. Puffing results from the cyclic blockage and blowout of the gas at the orifice. The dynamics of the system depend on both the experimental flow conditions and the dynamics and control of the gas delivery system. Figure 7b presents a time-series of gas pressure at the orifice to illustrate the puffing phenomenon captured by the simulation, where a length of the inlet pipe is included in the simulated geometry allowing for the flow to interact with the connection at the orifice. Based on the CFD the Strouhal number ($\mathrm{St} = fD_i/U_\infty$) of this puffing was found to be ~0.29. Albeit presumably due to a different physical mechanism, the gas-liquid interface with periodic structures due to the puffing has an appearance reminiscent to that seen on the interface of a cavitating jet in a cross-flow (Brandner *et al.* 2015). Figure 9 also reveals that effective jet diameter D_E at the jet exit is much larger than the orifice diameter D_i. Figure 10 presents of plot of the D_E as function of jet to cross-flow velocity ratio, and for all conditions D_E has uncertainty of ± 3 mm. We also note that the orifice diameter does not necessarily scale the geometry of the jet, even near the location of injection. There is also a clear dependence on boundary layer thickness, as a thinner boundary layer will present higher average cross-stream flow momentum to the exiting gas stream, and the expected outcome is corroborated based on comparison of Case A1 *vs.* D results for which also the numerical results compare favorably to experimental data, as seen in Table 3. It is interesting to note that the data collapses, if the cross-flow velocity is scaled with the ratio of the turbulent boundary layer thicknesses.

4.2 *Formation of the gas-filled branches*

Figure 11 shows the computation with buoyancy for the conditions otherwise similar to those shown in Figure 8 without buoyancy. The influence of buoyance leads to a significantly different topology of the gas pocket. The effect is evident within a few D_E downstream of the orifice, as the liquid flowing around the cavity begins to move up toward the flow boundary, bisecting the gas pocket, and creating two flow branches. Without gravity, the gas pocket forms and develops into a long slender cavity with the shape of a semi-ellipsoid. However, as seen in more detail in Figure 11 (b), (d) and (f), with gravity acting normal to the flow direction, and hence buoyancy moving the gas toward the flow boundary, the gas pocket is bisected, forming the two stable branches (note: the pressure peak on surface at bifurcation location seen in Figure 11 (b)). This topology was observed experimentally for the wide range of flow conditions of the present study. At speeds ≥ 2 ms^{-1}, the leading edges of the gas branches were usually well defined and straight. The chord length of the branches was also nominally constant, until entrainment of gas away from the branches led to their gradual diminution.

4.3 *Sweep angle of the gas branches*

The sweep angle, φ, is the angle between the plane perpendicular to the cross-flow and leading edge of the branch. The angles of both branches were measured from multiple images. The uncertainty was estimated as $\pm 1.5°$ and is principally attributed to

the fluctuations of the edge of the gas branch that is related to the puffing discussed previously. Figures 12 through 15 illustrate how the sweep angle, φ, changes with varying cross-flow speed U_∞, jet volume flow rate Q_i, injection orifice diameter, D_i, and injection angle β. The sweep angle significantly varies with varying cross-flow speed, jet volume flow rate, and, to a lesser extent, the injection hole diameter and injection angle. Figure 16 presents plots of φ *versus* Q_i for varying U_∞ for the three nominal orifice diameters of 5, 10, and 20 mm, for $\beta = 90°$. The sweep angle is primarily a function of the free-stream speed, with the angle increasing with increasing speed. Conversely, for a fixed value of U_∞, the sweep angle decreases with increasing gas flow-rate, Q_i.

Variation in the orifice size, D_i, and injection angle, β, suggest that that the gas exit velocity and momentum in direction of the cross-flow has a secondary, but discernable, influence on the sweep angle. A higher exit velocity (*i.e.* smaller orifice for fixed volume flux) and higher injection angle (*i.e.* increased momentum against cross-flow) led to a smaller sweep angle for a given volume flux of gas. Figure 17 shows the effect of gas injection angle, and in the extreme case of $22.5^o < \beta < 157.5^o$ a nearly 6^o difference is observed, which approximately the same as effect of changing the gas volume flow rate by a factor of five in 3 ms^{-1} liquid cross-flow.

4.4 *Chord length of the gas branches*

The average chord of the gas branch, C, was measured along several span-wise segments across the thickness part of the branch, and the measurement uncertainty of $\pm$ 5 mm is primarily due to fluctuations of the edge of the gas branches. Figures 12 through 15 also illustrate the changes in C for varying cross-flow speed U_∞, jet volume flow rate Q_i, injection angle β, and injection orifice diameter, D_i. The chord length C is a strong function of the volume flow rate, Q_i, the orifice diameter, D_i, and the boundary layer thickness, δ. Figure 18 present plots of C versus Q_i for varying U_∞ for the three nominal orifice diameters of 5, 10, and 20 mm and for β = 90°. The dominant trends are increasing C with Q_i. And Figure 19 illustrates the effect of β, with a clear trend of increasing chord with increasing momentum of gas injection against cross-flow. Similar to what was observed for angle, φ, the chord length is not independent of δ, D_i, and β, but the dominant variables are again Q_i and U_∞.

4.5 *Topology of the gas pocket at low free-stream speed*

Observation of the jet-and-branch topology show consistent trends except at the lowest cross-flow speed examined. Figure 20 compares the topologies for changing cross-flow speed ranging from U_∞= 1 to 3 ms^{-1}. At the lowest speed, the branches barely form and have irregular leading edge and chord length. But, as the speed increases, they become distinct, straight, and more uniform in chord. This phenomenon is related to the relative importance of surface tension in the flow and is discussed in Section 6.4.

5. The Computed Flow Within and Around the Cavities

The flows for a subset of the experimentally observed conditions are computed, and their parameters are listed in Table 3. Also shown are the computed parameters D_E, φ, C, and the maximum thickness of the gas branch, e, along with the experimentally observed

quantities for the similar conditions listed in parenthesis. Overall, the features of the experimentally observed flow are captured well by the computations, as evident from the comparison in figure 21. Figure 21(a) presents a comparison between an image of the observed flow along with the cavity outline from the computation demonstrating the very good match between the two. The stream-wise evolution of the cavity observed in the experiment is generally well captured by the computational prediction. The only significant difference is observed on the detailed appearance of the instantaneous cavity surface interface, with the computational interface being rougher than the experimentally observed interface. It is important to recall that the numerical simulations are performed on a grid with finite resolution, and the error due to the discretization may play a role in the small differences that are present between the experimental observations and the numerical predictions.

Figure 22 shows the computed topologies for all conditions listed in table 3, as well as comparisons to photos from experiments. We also see not only that the variation of sweep angle and chord is well captured by the CFD, but we can also observe the side profiles of the cavities. From the side profiles we see that the 'hump' height varies as the gas momentum compared to that of the cross-flow, and is influenced to a lesser extent by the boundary-layer thickness. Also evident is that the magnitude of the pressure peak at bifurcation location varies approximately proportionally to hump height.

In the next sections, we use U_∞ and δ to scale length and velocity. The static pressures will be scaled either by eqn. (4.1) or by the following relationship

$$p = \frac{P}{P_\infty + \rho_\infty g y} - 1 \qquad (5.1)$$

where P is the computed average static pressure, and y is the distance from the flow boundary (in direction along gravity vector). With this normalization, we can show how the gas pressure within the cavity varies with respect the static pressure in the fluid far from the injection location. Figure 23 illustrates the sections of the flows that will be presented. Section PX is the plane of symmetry parallel to the mean flow direction; Sections PY are the planes perpendicular to the surface and the mean flow direction; Section BX is the plane parallel to and centered on the gas branch; and Sections BY are planes normal the gas branch.

5.1 *The basic cavity flow*

Figures 24 present contours of the time-averaged (a) static pressure, p, and (b) the in-plane velocity magnitude, $|\boldsymbol{u}|/U_\infty$, on the PX plane for Cases A1 and D. Figure 24(c) is an instantaneous realization of the pressure field. When $p < 0$ at the gas-liquid interface, buoyancy will tend to move the gas back toward the plate. At the jet exit, the pressure at the gas-liquid interface is such that $p >> 0$ and matches the stagnation pressure of the incoming liquid flow. Along the interface of the cavity, p decreases and the initial gas pocket begins to close and form the branches. The influence of the gas volume flux can be seen through the change in the shape of the initial gas pocket. With the higher gas flux the hump is taller and the upward momentum of the liquid following the contour of the hump is sufficient to bifurcate the gas pocket, as also seen in figure 22. Recall that the branches form as the freestream liquid around the gas cavity returns to the flow boundary

along the plane on symmetry and bifurcates the gas pocket. This is illustrated in figures 22 and 25(b and c) that show the surface pressures for the case A1 (also presented in figure 11). A high-pressure region is observed at the location of cavity bifurcation that results from the impingement of the liquid onto the wall boundary. Whether the region between the gas branches is filled with gas (delta type cavity) or liquid on the surface (lambda type) is of importance if the goal is to form an air layer evenly covering the surface. Figure 25 (c) also shows the large flow structures that form in front of the gas injection location, and persist far downstream. The vortex structures are visualized with the second invariant of the velocity-gradient tensor, commonly referred to as the *Q*-criterion (Hunt *et al* 1988). These structures modify the boundary layer 'seen' by the branch from one with $u/U = (y/\delta)^{1/n}$ power-law shape best fitted with $n \sim 8$ to $n \sim 5$. This can explain how the manner in which the gas is introduced into the flow can affect the equilibrium sweep angle far downstream, and other detail discussed in section 6. Figure 25(a) also shows the mean velocity field, and in particular, the manner in which the turbulent mean profile that is applied on the inlet persists downstream until it is modified by the cavity.

Figure 26 presents a series PY planes illustrating the time-averaged in-plane velocity magnitude for the case A1. The planes start upstream of the injection location and move downstream toward the formation of the branches, at the location where the liquid impinges on the surface. Figure 27 presents the normalized pressure, *p*, to illustrate the influence of buoyancy on the development of the branches. Away from the gas injection site the cavity is at a constant pressure, far from the branches the pressure varies due to buoyancy as $\rho_\infty g y$. However, near the cavity the pressure is below $\rho_\infty g y$, as the flow accelerates locally.

5.2 *Flow around and within the stable gas branches*

Once the two branches have been formed, they maintain a near equilibrium topology as they extend downstream from the cavity injection location with both a fixed gas sweep angle and chord length. Figure 28 presents the flow along the branch in the plane BX, and this shows that the flow along the center of the branch reaches equilibrium within ~$5x'/\delta$ distance from the injection location. The flow over the branch is reminiscent of the flow over a long swept wing, and we can use the concepts of incompressible swept wing theory. Figure 29 presents the time-averaged static pressure, *p*, and flow speed and velocity vectors, for the case A1 at the location x'/δ where the branch has reached a near equilibrium shape. The slices of figure 29 more clearly show there is only minimal variation in the branch shape until it is impinged on the exit of the computational domain. Experimentally, the variation along the branch was significant in cases where notable amounts of gas were entrained all along the closure of the branches.

5.3 *Influence of freestream speed and boundary layer thickness*

The experimental observations suggested that the freestream speed and boundary layer thickness both significantly influence the topology of the gas branches, and this was explored computationally. Cases B and C were computed with U_∞= 2 and 4 ms^{-1}. Figure 30 presents the (a) time-averaged static pressure, *p*, (b) the flow speed and velocity

vectors at the location x'/δ where the branch has reached a near-equilibrium shape. Besides the obvious change in angle, the branches become significantly smaller in both chord, *C*, and height, *e*. Inspection of the average gas velocity along the branch shows good correlation with $U_\infty \sin(\varphi)$, as well as some dependence on *e*, and this notable observation is discussed further in section 6.

The effect of incoming boundary layer thickness was examined by computing Case E with $1/3\delta$ of Case A1. Figures 31 and 32 present the time-averaged static pressure, *p*, and the flow speed and velocity vectors for the case E, respectively. While the chord changed modestly, a significant difference in branch thickness is observed. We should also note the difference in pressure immediately upstream of both the injection and branches, as was seen most clearly in figure 22, and is likely due to change in stagnation pressure and relative strength of large structures (*i.e.* junction vortex) observed in figure 25. For these cases, we also find that the average gas velocity along the branch shows dependence on *e*, in addition to $U_\infty \sin(\varphi)$, as will be discussed in the next section.

6. Scaling of the Gas Branch Topology

The sweep angle, chord length, and general gas branch topology were determined for a range of conditions in order to develop scaling relationships. We can define five non-dimensional groups to scale both of the dependent variables φ and *C,* that are derived from the eight independent parameters, U_∞ δ, Q_i, D_i, β, ρ_∞, υ_∞ and g. We assume that the gas is incompressible with a density much less than the liquid. The influence of surface tension is discussed separately in section 6.4. The five groups of independent parameters can be chosen as the Froude number based on the boundary layer thickness Fr = $U_\infty/\sqrt{g\delta}$, the Reynolds number based on the boundary layer thickness, Re = $U_\infty\delta/\upsilon_\infty$, the scaled gas volume flow rate $Q^*= Q_i/U_\infty\delta^2$, the scaled gas injection velocity $U^* = U_i/U_\infty$, and the angle of the gas injection β. Note that $U_i = Q_i/\pi(D_i/2)^2$. The experimental ranges of these non-dimensional parameters are presented in Table 4. Henceforth, we will exclude the data collected for U_∞< 2 ms^{-1} since these gas pockets that have less stable and regular gas branches, and we will first focus on scaling for the case of fixed gas injection angle $\beta = 90^o$ (*i.e.* wall-normal injection). We will attempt to scale sweep angle, φ, and normalized chord length, C/δ, with the four parameters Fr, Re, Q^*, and U^*.

6.1 *Power law scaling*

Figure 33 presents $\cos\varphi$ as a product of four non-dimensional groups raised to a exponents derived from nonlinear regression. The scaling successfully groups the data with the following equation:

$$\cos\varphi \cong 1.012\,\mathrm{Re}^{-0.037}\mathrm{Fr}^{-1.089}Q^{*0.267}U^{*0.137} \qquad (6.1)$$

A linear regression of this function has a correlation of 0.94. From (6.1) we see that the Froude number has the largest influence on the sweep angle, with the angle decreasing with increasing Fr. A similar regression is shown in Figure 34 for C/δ:

$$\frac{C}{\delta} \cong 1.3 \cdot 10^{-4} \ \ \mathrm{Re}^{0.84}\mathrm{Fr}^{-0.67}Q^{*0.57}U^{*0.23} \tag{6.2}$$

Here, the scaling has a somewhat reduced correlation of 0.87. Based on the exponents found from regression, the cavity chord, C/δ, is strongly related to the rate of volume injection, as expected. However, the chord is also significantly influenced by the Froude number, injection velocity, and Reynolds number. Next, we will present a physical basis for these observed scaling.

6.2 *A simplified model of the flow around the gas branch*

A simplified model of the flow around a single gas branch can help illuminate the basic flow processes that lead to the formation of such a straight and stationary gas pockets. We expect that the drag of the long gas pocket is proportional to its height, e, the boundary layer thickness, δ, flow static pressure, P_∞, and the pressure of the gas within the cavity, P_C. If we consider the component of the drag force perpendicular to the leading edge of the gas branch, D, the net force is given by

$$D \sim \frac{1}{2} C_D e \ \rho_\infty \left(U_\infty \cos\varphi \left(\frac{e}{\delta}\right)^{\frac{1}{n}} \right)^2 - (P_c - P_\infty) e \tag{6.3}$$

where C_D is a drag coefficient and $U_\infty cos\varphi$ is the magnitude of the velocity component perpendicular the leading edge scaled by the depth the cavity penetrates the boundary layer, e/δ, and where $1/n$ is the exponent of the boundary layer profile power law. If we assume that the drag coefficient is a weakly decreasing function of the Reynolds number based on the cavity thickness, then

$$C_D = C_{DO} \left(e U_\infty \cos\varphi \left(\frac{e}{\delta}\right)^{\frac{1}{n}} / \nu_\infty \right)^{-m} \tag{6.4}$$

where $m > 0$ is a constant. A cavitator is formed by the leading edge of the gas pocket, but it is not fixed to the surface. Therefore, in order to have a stationary gas pocket in the lab frame of reference, the net drag force on the gas pocket must be zero. Setting $D = 0$ in (6.3) yields the force equilibrium condition:

$$0 = \frac{1}{2} C_D \rho_\infty \left(U_\infty \cos\varphi \left(\frac{e}{\delta}\right)^{\frac{1}{n}} \right)^2 - (P_c - P_\infty) \tag{6.5}$$

The average cavity pressure, P_C, will be related to the cavity height, volume rate of the injected air and the rate of gas entrainment at the local cavity closure and the terminus of the branch at the farthest downstream extent of the gas pocket. Without direct measurements of the pocket pressure, a relationship for P_C must be prescribed. We will therefore assume that P_C in the gas branch is on the same order of, but less than, the

hydrostatic pressure in the surrounding liquid at a depth of the branch maximum thickness, *e*:

$$P_C = P_\infty + K_1 \rho_\infty g e \quad \text{where} \quad 0 < K_1 < 1 \tag{6.6}$$

Finally, we need a relationship between the gas branch height, *e*, and the volume flow rate of gas, Q_i. We can develop such a relationship if we assume that a fraction K_2 of the injected air flows through branches $Q_{branch} = Q_i/2K_2$, where K_2 would be unity for a Lambda with no gas leakage between the branches. We can also assume that profile of the branch approximates a half ellipsoid such that branch chord

$$c(y) = C\sqrt{1-(y/e)^2} \tag{6.7}$$

And, finally, we will assume that the gas flow speed within the branch is equivalent to the branch-normal speed of the liquid at same location from the plate surface, *y*, such that

$$u_{branch}(y) = U_\infty \sin\varphi \, (y/\delta)^{1/n} \tag{6.8}$$

The, the expression for the gas flux in the branch becomes:

$$\frac{Q_i}{2} = K_2 \int_0^e U_\infty \sin\varphi \, (y/\delta)^{1/n} C\sqrt{1-(y/e)^2}\, dy \tag{6.9}$$

For **Re**$(1/n) > -1$ this yields

$$e = \delta \left[\frac{2}{\sqrt{\pi}K_2 S(n)} \frac{\delta Q^*}{C \sin\varphi}\right]^{\frac{n}{n+1}} \tag{6.10}$$

Where $S(n) = \Gamma(\frac{n+1}{2n})/\Gamma(\frac{4n+1}{2n})$. (Note: for the branch thickness, e, and angle, φ, found from the CFD the average gas velocity in the branch based on equation (6.9) with K_2=1 *vs.* CFD match well, yielding 2.08 *vs.* 2.08 and 2.53 *vs.* 2.51 m/s, for cases A1 and E, respectively.)

Equations (6.4), (6.5), (6.6), and (6.10), can now be combined to develop a relationship between the Re, Fr, Q^*, and φ:

$$\mathrm{Re}^{-m}\, \mathrm{Fr}^2 \cos^{2-m}\varphi \; Q^{*r} \left(\frac{C}{\delta}\sin\varphi\right)^{-r} = \frac{2K_1}{C_{DO}}\left[\frac{\sqrt{\pi}K_2}{2} S(n)\right]^r \tag{6.11}$$

where

$$r = \frac{(2-n)-m(1+n)}{n+1} \tag{6.12}$$

This scaling does not include the one additional parameter associated with the wall-normal injection process, the gas injection velocity U^*. It is therefore instructive to plot the scaling suggested by equation (6.11) as a function of $U^* = U_i/U_\infty$. This is shown in figure 35, where the function

$$\mathrm{Re}^{-\hat{m}}\,\mathrm{Fr}^2\,\cos^{2-\hat{m}}\varphi\;Q^{*\hat{r}}\left(\frac{C}{\delta}\sin\varphi\right)^{-\hat{r}} \tag{6.13}$$

is plotted *versus* U^*. The data has the best linear fit for regression constants $\hat{m}$ =0.40 and $\hat{r}$ =-0.79 with a correlation of 0.48. Note that a positive value of $\hat{m}$ suggests that the drag coefficient of the cavity would be *decreasing* with increasing Reynolds number, as we would expect. From (6.12) we would also get n = 3.9, which can be compared to the experimentally observed value of n ~7. The decreased n would physically translate to a more gradual rate of velocity gradient in front of the branches. Indeed, from the CFD, as discussed in conjunction with figure 25, we observed the large junction vortex type flow structures that modified the flow seen by the branch, and in the CFD we observed these to drop n from ~8 to ~5, which would seem to support the idea that n seen by the branches in the experiment may have well been ~4.

It is important to note, however, that the scaling does not lead to a constant value as a function of U^*, which we would expect if the force balance around the branch is independent of the gas injection process except for the gas volume flux. However, we see an approximately linear dependence on the relative injection velocity such that with increasing U^* the magnitude of equation (6.13) increases.

To explore this further, we introduce the influence of the gas injection velocity into the scaling as

$$\mathrm{Re}^{-\hat{m}}\,\mathrm{Fr}^2\,\cos^{2-\hat{m}}\varphi\;Q^{*\hat{r}}\left(\frac{C}{\delta}\sin\varphi\right)^{-\hat{r}}U^{*\hat{q}} \tag{6.14}$$

The regression for this function is shown in figure 36 as a function of U^* with $\hat{m}$ = 0.73, $\hat{r}$ = -0.82 and $\hat{q}$ = 0.79. These data show better grouping, and again the positive value of $\hat{m}$ suggests that the drag coefficient of the cavity would be decrease with increasing Reynolds number, as we would expect. This new scaling also suggests that the details of the gas injection process influence the equilibrium topology of the gas branch. We would therefore expect that the gas injection angle would also play a role. To explore this, the U^* is scaled by $\sin\beta$

$$\mathrm{Re}^{-\hat{m}}\,\mathrm{Fr}^2\,\cos^{2-\hat{m}}\varphi\;Q^{*\hat{r}}\left(\frac{C}{\delta}\sin\varphi\right)^{-\hat{r}}(U^*\sin\beta)^{\hat{q}} \tag{6.15}$$

U^* is shown in figure 37 as a function of (6.15) including the data for cases where $\beta \neq 90^o$. These data for $\beta = 90^o$ follow the trend as well, but there remains some noticeable scatter for the $\beta \neq 90^o$ data, that indicates the simple scaling does not fully capture how the methods of gas injection (modifying both the hump height and large junction vortex type flow structures) effects the overall flow, leading to a different equilibrium for the branches.

The physical model discussed above presents the trends observed in the scaled data (Section 6.1). The scaling from equation (6.13) can be combined with that of equation (6.2) to create the scaling if we assume $(\sin\varphi)^{-p} \approx 1$. Recall that this scaling does not include the influence of U^*, but it will be introduced into this scaling solely through its factor in the open regression. Combining equations 6.2 and 6.13, the model scaling based on the drag balance around the branch yields

$$\cos\varphi \sim \mathrm{Re}^{-0.16}\mathrm{Fr}^{-0.92}Q^{*0.21}U^{*0.51} \tag{6.16}$$

This can be compared with original open regression for the sweep angle

$$\cos\varphi \sim \mathrm{Re}^{-0.037}\mathrm{Fr}^{-1.1}Q^{*0.27}U^{*0.14} \tag{6.1}$$

The exponents for Fr and Q^* are similar, with the Froude number being the dominant parameter. The scaling based on the model over-predicts the influence of Re and U^*. And, the scaling would suggest a power law profile of $n \sim 4$ (equation 6.12) for the boundary layer (*i.e.* a more gradual boundary layer profile). Re and U^* are still significant and necessary parameter for both relations.

The question, therefore, is how the process of injection could be coupled to the drag balance around the branch flow far downstream from the injection location. One possibility already discussed is that the gas injection process could cause diversion of the gas from the branches (when delta topology is achieved) thus leading to only a fraction of the gas flowing through each branch with the remainder flowing between the branches. A second possibility is that the injection process can lead to a change in the liquid flow upstream of the gas pockets. Examination of the computed flow upstream of the branches indicates that presence of a junction vortex, visualized in figure 25, that formed at the stagnation region around the jet. The vortex flow parallel to and upstream of the gas branches and, as such, can modify the momentum balance described in equation (6.5), modifying the effective drag coefficient with increasing vortex strength. Then, the drag coefficient would be a function of not only the Reynolds number but also the strength of the junction vortex. The vortex strength would, in turn relate to a U^* and β. Note that the quantity $\rho_\infty ge \approx 10^2$ Pa, therefore only a small modification of the pressure upstream of the branch may be sufficient to modify the drag balance.

We conducted an additional experiment to examine how the formation of a potentially stronger junction vortex would affect the formation of the gas branches, if all other parameters are kept constant. To do this, we extended a portion of the outlet tube to create a solid boundary upstream of the injection location, as shown in figure 38. During the experiment, the presence of the barrier led to a stagnation flow ahead of the gas injection, and a path for the gas to extend farther into the free-stream before reattaching to the surface to form the gas pocket. Examination of the resulting flows showed that, for fixed Fr, Q^* and U^*, the presence of the barrier led to a *decrease* of the sweep angle (increase in $\cos\varphi$) and increased tendency towards lambda type gas pocket topology. This is consistent with the hypothesis that the formation of a stronger junction vortex would lead to a reduction of the drag coefficient of the branch and a resulting decrease in the equilibrium sweep angle, and with taller hump promoting lambda topology.

6.3 *Stability of the gas branch*

With a relationship developed between the sweep angle and the drag force on the gas branch, we can examine if our simplified model predicts a stable, straight gas branch.

Given the force balance of equation (6.3), we can take the derivative of the drag force D with φ around the point of force equilibrium:

$$\left(\frac{\partial^2 D}{\partial \varphi^2}\right)_{D=0} \propto 2\sin^2\varphi - 2\cos^2\varphi + \cdots \tag{6.17}$$

Since 45 ^{o} < φ < 90^{o}, the sign of $(\partial^2 D/\partial\varphi^2)_{D=0}$ is always greater than zero, implying that a restoring force exists that resists perturbation of the branch. Hence, when there is a positive perturbation of the sweep angle, a net negative drag force occurs, and this results in the branch returning to its equilibrium position. Similarly, if the sweep angle is reduced, the drag on the branch increases, and it is pushed back. Thus, the simplified model confirms that the gas branch, once formed, will change in sweep angle until the equilibrium position is achieved and will resist perturbation.

6.4 *Consideration of surface tension*

The previous discussion has illustrated how the flow around the gas branches is dominated by inertia and buoyancy. However, cases with lower cross-flow speed ($U_\infty \leq$ 1 ms^{-1}) do not exhibit gas branches with strongly defined and straight leading edges. In these cases, the surface tension at the air-liquid interface may be a consideration. If we balance the dynamic pressure and pressure due to surface tension at cross section of the branch, we find that:

$$\frac{1}{2}\rho_\infty\left(U_\infty \cos\varphi\left(\frac{\kappa}{\delta}\right)^{1/n}\right)^2 \sim \frac{S}{\kappa} \tag{6.18}$$

where S = 0.072 Nm^{-1} is surface tension of water-air interface and κ is the curvature at the leading edge of the branch. Modifying this equation to define the Weber number, We, we find the following relation:

$$\frac{\rho_\infty {U_\infty}^2 \kappa}{S} = \mathrm{We} \sim 2\cos^{-2}\varphi\left(\frac{\kappa}{\delta}\right)^{-2/n} \tag{6.19}$$

The leading edge curvature is on the order of $\kappa/\delta \sim 10^{-1}$. At speeds where $U_\infty > 3$ ms^{-1}, the sweep angle varied between, 75^{o} < φ < 88 ^{o} making 0.12 < $cos^2\varphi$ < 0.3 and therefore increasing the range of Weber numbers to 50 < We < 3200. But, at the lowest flow speed of $U_\infty = 1$ ms^{-1}, the sweep angle varied between, 55^{o} < φ < 70 ^{o}, making 0.12 < $cos^2\varphi$ < 0.33. Then, the range of Weber numbers is reduced to 12 < We < 33. This scaling therefore suggests that at the lowest speeds, we are approaching the conditions were the We ≈ O(1), and surface tension can no longer be neglected.

6.5 *Transition from Delta to Lambda topology*

The data presented in Figure 39 show the transition from one topology type to another is sensitive to the boundary layer, the liquid cross-flow velocity, the momentum of the gas normal to the flow, and the volume flux of gas. For sufficiently high Fr, increasing

Q^* or setting $\beta = 90^o$ increases the degree to which the gas jet penetrates the free-stream flow, and we would expect that this would increase the likelihood that distinct gas branches (*i.e.* a lambda topology) would form as the liquid flow impinges back on the plate surface. Hence, the delta-lambda transition, is likely to depend on the initial mechanism that bifurcates the cavity and sets the angle and chord length. Indeed, if the gas hump height is modified by changing the gas injection angle, β, or is rendered quasi-independent of the gas injection flow rate by placing a solid obstacle upstream of the orifice, the delta-to-lambda transition conditions shift to different values of Fr and Q^*.

7. Conclusions

The flow of a gas jet beneath a flat surface and into a liquid cross-stream was examined both experimentally and computationally. Unlike flow configurations where body forces can be neglected, the gas jet is strongly influenced by the presence of buoyancy and is driven toward the plate surface as it convects away from the injection location. Then, the gas pocket is cleaved into two gas pockets that form straight branches at a particular sweep angle relative to the incoming flow. Examination of the data indicates that the dominant parameter of the flow is the Froude number based on the thickness of the incoming boundary layer and the non-dimensional volume flow rate of the injected gas. The gas branches are nominally straight and stable, as they represent an equilibrium state balancing drag force on them due to the convection of the boundary layer over the gas pocket against the force on the interface due to the gas pressure within the branch. Because the branches are immersed in the boundary layer, the boundary layer thickness is an important parameter. Increase in the free-stream speed leads to an increase in the sweep angle of the branches, as the fraction of the stagnation pressure required to balance the cavity pressure decreased. The volume flux of the injected gas changes the chord length and height of the branches and hence, secondarily, the equilibrium sweep angle.

These observations of the cavity topology can be related to the balance of drag around the stable gas branch. This, in turn, is related to the impinging speed of the boundary layer flow, the cross-sectional area of the branch and the gas pressure within it. The cavity pressure is on the order of the local buoyancy-induced static pressure at the deepest extent of the pocket, and the geometric cross-section of the branch is strongly related the overall gas volume flux moving through the branch at a component of the boundary-layer speed. In order for a stable branch to form, there must be a balance of the drag forces on the cavity. And, to achieve this, the branch must rest at a particular sweep angle such that it intercepts the necessary parallel and tangential component of the incoming flow velocity to produce equilibrium. However, the process of gas injection can modify both the amount of gas that ultimately flows though the branches as well as the local liquid flow that impinges around the leading edge of the gas branches. Therefore, the scaling of branch sweep angle and chord length is dependent on both the free-stream parameters Fr and Re, the rate of gas injection, Q^*, and the process of gas injection related to both U^*, and β.

The method of gas injection (*e.g.* injection angle and orifice size) had the strongest influence on the cavity topology. However, scaling the near-injector gas pocket was problematic. With increasing flow speed, the relative effect of buoyancy will be reduced, and we would expect to see the flow evolve to that described by Pignoux (1998), Vigneau

et al. (2001a), and Vigneau *et al.* (2001b) for the injection of gas into a downward flowing vertical stream. Hence, we consider the Froude numbers range of the present study to be moderate. However, in the present orientation and in the presence of gravity, even with increased flow speed with sufficient distance from the injector, buoyancy will ultimately flatten and potentially bisect the gas cavity, if it had not already been broken up by turbulent action at the cavity interface.

Acknowledgements

This work was funded in part by the National Research Foundation of Korea (NRF) under grant N014691 and by the Office of Naval Research under grant N00014-14-1-0292, Dr. Ki-Han Kim program manager. This work used the Extreme Science and Engineering Discovery Environment (XSEDE), which is supported by National Science Foundation grant number OCI-1053575.

REFERENCES

ABDELWAHED, M. S., & CHU, V. H. 1978 "Bifurcation of Buoyant Jets in a Crossflow", *Verification of Mathematical and Physical Models in Hydraulic Engineering*, American Society of Civil Engineers, 819-826.

BRACKBILL, J. U., KOTHE, D. B. & ZEMACH, C. 1992 "A continuum method for modeling surface tension", *Journal of Computational Physics*, **100**, 335–354.

BRANDNER, P. A., PEARCE, B. W. & DE GRAAF, K. L. 2015 "Cavitation about a jet in crossflow", *Journal of Fluid Mechanics*, **768**, 141-174.

CECCIO, S. L., 2010 "Friction Drag Reduction of External Flows with Bubble and Gas Injection", *Annual Review of Fluid Mechanics*, **42**, 183-203.

CHOI, K. W., Lai, C. C., & Lee, J. H. 2015. "Mixing in the Intermediate Field of Dense Jets in Cross Currents", *Journal of Hydraulic Engineering*, **142**(1).

ELBING, B., MÄKIHARJU, S. A., WIGGINS, A., PERLIN, M., DOWLING, D., & CECCIO, S. L. 2013 "On the Scaling of Air Layer Drag Reduction", *Journal of Fluid Mechanics*, **717**, 484-513.

ELBING, B. R., WINKEL, E. S., LAY, K. A., CECCIO, S. L., DOWLING, D. R., & PERLIN, M., 2008 "Bubble-Induced Skin-friction Drag Reduction and the Abrupt Transition to Air-layer Drag Reduction", *Journal of Fluid Mechanics*, **612**, 201- 236.

FRANC, J.-P. & MICHEL, J-M., 2004. "Fundamentals of Cavitation", *Kluwer Academic Publishers*.

HIRT, C. W. & NICHOLS, B. D. 1981 "Volume of fluid (VOF) method for the dynamics of free boundaries", *Journal of Computational Physics*. **39**, 201–225.

HUNT, J. C. R, WRAY, A. A. & MOIN, P. 1998 "Eddies, streams, and convergence zones in turbulent flows". *In Proceedings of the Summer Program*, 193–208. Center for Turbulence Research.

INSEL, M., GOKCAY, S., & HELVACIOGLU, I. H., 2010 "Flow Analysis of an Air Injection Through Discrete Air Lubrication", *International Conference on Ship Drag Reduction*, paper No. 13.

LEE, I.-H. R., 2015 "Scaling of Gas Diffusion into Limited Partial Cavity and Interaction of Vertical Jet with Cross-flow beneath Horizontal Surface", *Ph.D. Thesis, University of Michigan.*

MAHESH, K., 2013 "The Interaction of Jets with Crossflow", *Annual Review of Fluid Mechanics*, **45**, 379-407.

MÄKIHARJU, S. A., PERLIN, M., & CECCIO, S. L. 2012 "On the energy economics of air lubrication drag reduction." *International Journal of Naval Architecture and Ocean Engineering*, **4**(4), 412-422.

PIGNOUX, S., 1998 "Structure interne d'un jet de gaz injecté perpendiculairement à une couche limite turbulente verticale d'eau", Ph.D. thesis, University of Poitiers, France.

REYNOLDS, W. C., PAREKH, D. E., JUVET, P. J. D., & LEE, M. J. D. 2003 "Bifurcating and blooming jets", *Annual Review of Fluid Mechanics*, **35**(1), 295-315.

SANDERS, W. C., WINKEL, E., DOWLING, D. R., PERLIN, M., & CECCIO, S. L. 2006 "Bubble Friction Drag Reduction in a High Reynolds Number Flat Plate Turbulent Boundary Layer", *Journal of Fluid Mechanics*, **552**, 353-380.

SCARDOVELLI, R. & ZALESKI, S. 1999 "Direct numerical simulation of free-surface and interfacial flow", *Annual Review of Fluid Mechanics*, **31**, 567–603.

TOWNS, J., COCKERILL, T., DAHAN, M., FOSTER, I., GAITHER, K., GRIMSHAW, A., HAZELWOOD, V., LATHROP, S., LIFKA, D., PETERSON., G. D., ROSKIES, R., SCOTT, J. R., WILKINS-DIEHER, N. 2014 "XSEDE: Accelerating Scientific Discovery", *Computing in Science & Engineering*, **16**, 62-74.

VIGNEAU, O., PIGNOUX, S., CARREAU, J.-L., & ROGER, F., 2001a "Influence of the wall boundary layer thickness on a gas jet injected into a liquid crossflow", *Experiments in Fluids*, **30**, 458-466.

VIGNEAU, O., PIGNOUX, S., CARREAU, J.-L., & ROGER, F., 2001b "Interaction of Multiple Gas Jets Horizontally Injected into a Vertical Water Stream", *Flow, Turbulence and Combustion*, **66**, 183–208.

WACE, P. F., MORRELL, M. S., & WOODROW, J., 1987 "Bubble formation in transverse liquid flow", *Chemical Engineering Communications*, **62**:1-6, 93-106.

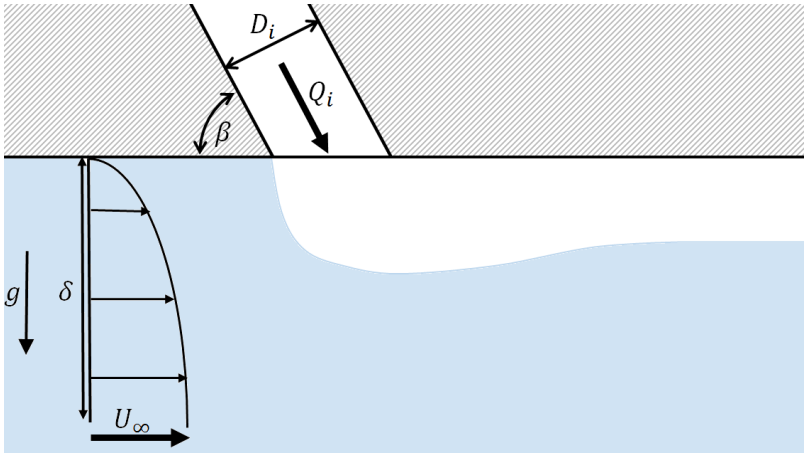

(a)

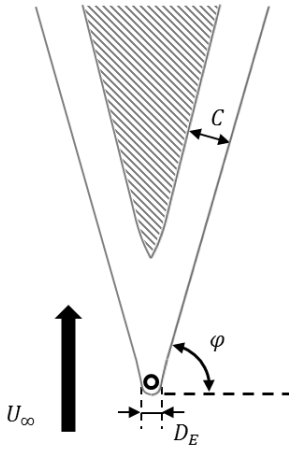

(b)

Figure 1: (a) a schematic diagram showing the side view of the flow near the point of gas injection, with the gas volume flow-rate at draft pressure, Q_i, the orifice diameter, D_i, the angle of injection, β, and the free-stream speed is U_∞; (b) a plan view of the basic cavity topology for gas injection into a liquid cross-stream when gravity is oriented such that buoyancy brings the gas toward the flat flow boundary showing the cavity sweep-angle, φ, the average chord length of the gas branch, C, and equivalent diameter of the jet D_E; Delta (Δ) type topologies have gas filled in between branches (area with cross hatching) and Lambda (Λ) types have little to no gas between the branches.

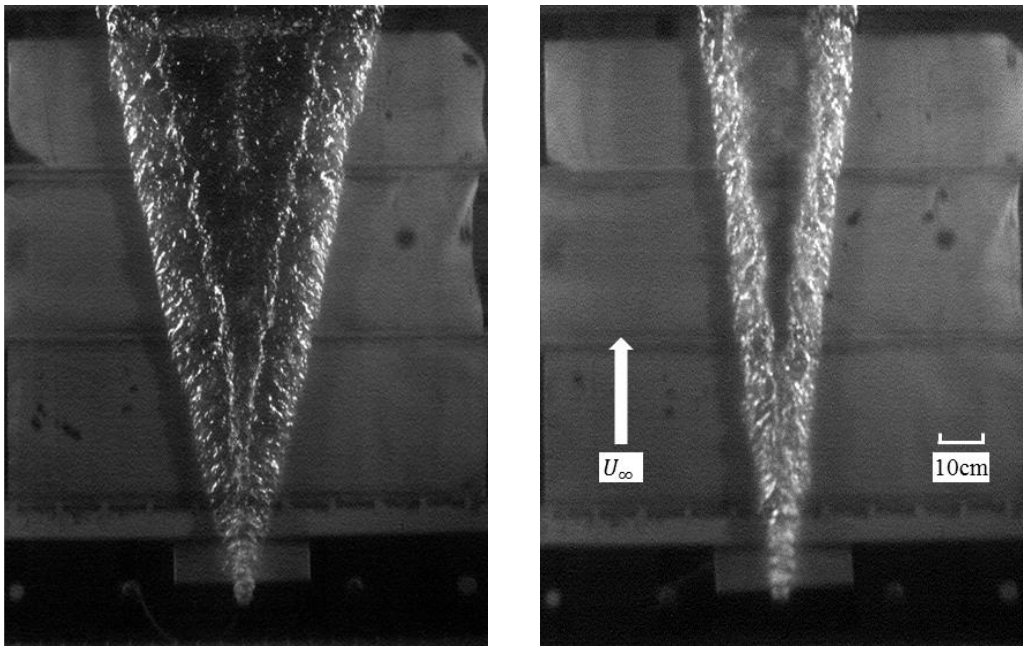

(a) (b)

Figure 2: The flow topology viewed from below; (a) the gas pocket with the Delta topology (*i.e.* gas layer between the branches) ($D_i \cong 5$ mm, $\beta = 112.5^o$, $U_\infty = 3.0$ ms^{-1}, $Q_i = 2.5\text{x}10^{-3}$ m^{3}s^{-1}, $\delta = 51$ mm), and (b) the Lambda topology (*i.e*. little to no gas between the branches) ($D_i \cong 10$ mm, $\beta = 90^o$, $U_\infty = 4.0$ ms^{-1}, $Q_i = 6.7\text{x}10^{-3}$ m^{3}s^{-1}, $\delta = 53$ mm). The flow direction is from bottom up.

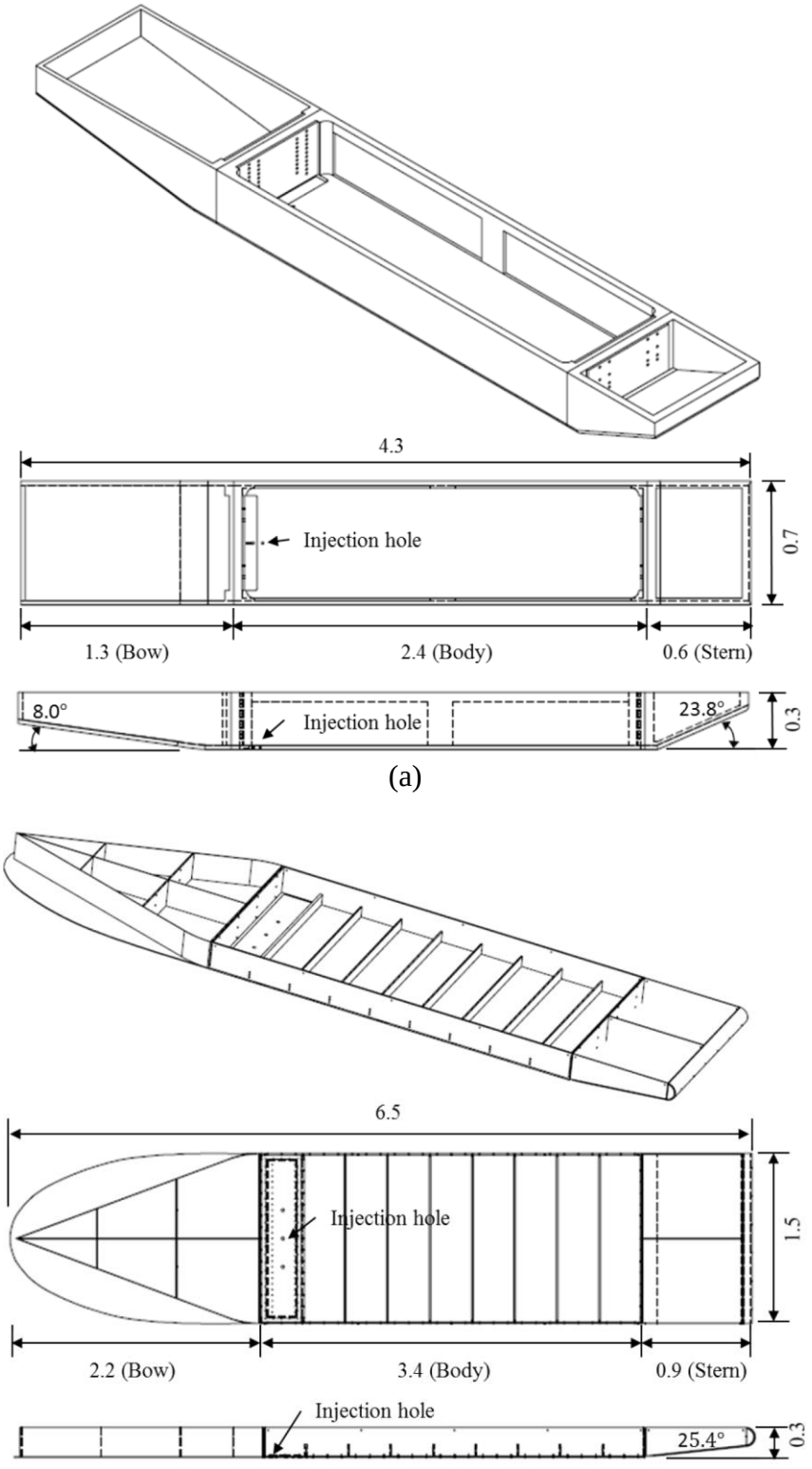

Figure 3: Sketches of (a) Barge I and (b) Barge II. All dimensions are in meters.

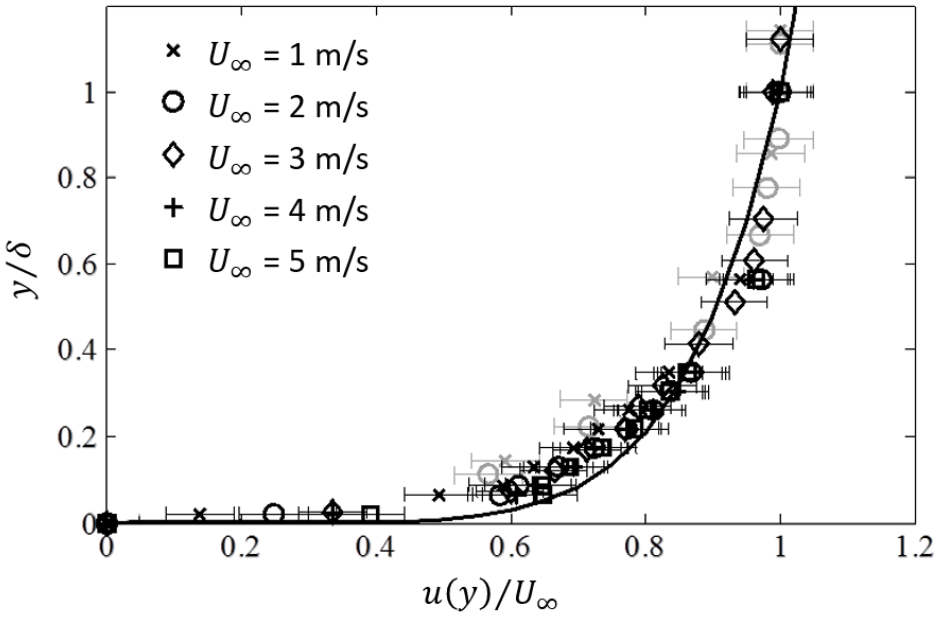

Figure 4: The boundary layer profiles measured at the location of gas injection for Barge I (grey symbols) and Barge II (black symbols); for Barge I, $15.8 \leq \delta_1 \leq 19.1$ mm over a speed range of $1 \leq U_\infty \leq 2$ ms^{-1}; for Barge II, $50.7 \leq \delta_2 \leq 57.4$ mm over a speed range of $1 \leq U_\infty \leq 5$ ms^{-1}. The solid line shows a 1/7th power-law.

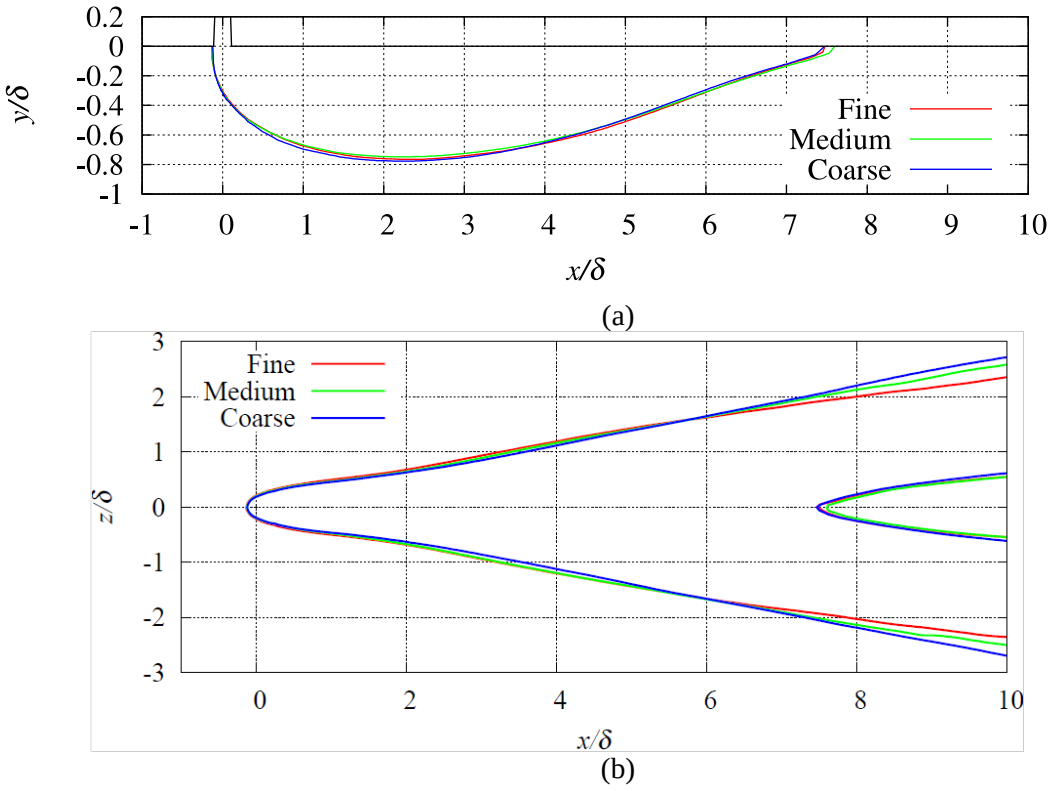

Figure 5: Time-averaged air-cavity profiles computed on three different grid resolutions for U_∞= 3.0 ms^{-1}, Q_i = 5.0x10^{-3} m^{3}s^{-1}, δ = 51 mm, D_i =10 mm, and β = 90^o (Case A) (a) center plane, and (b) plate.

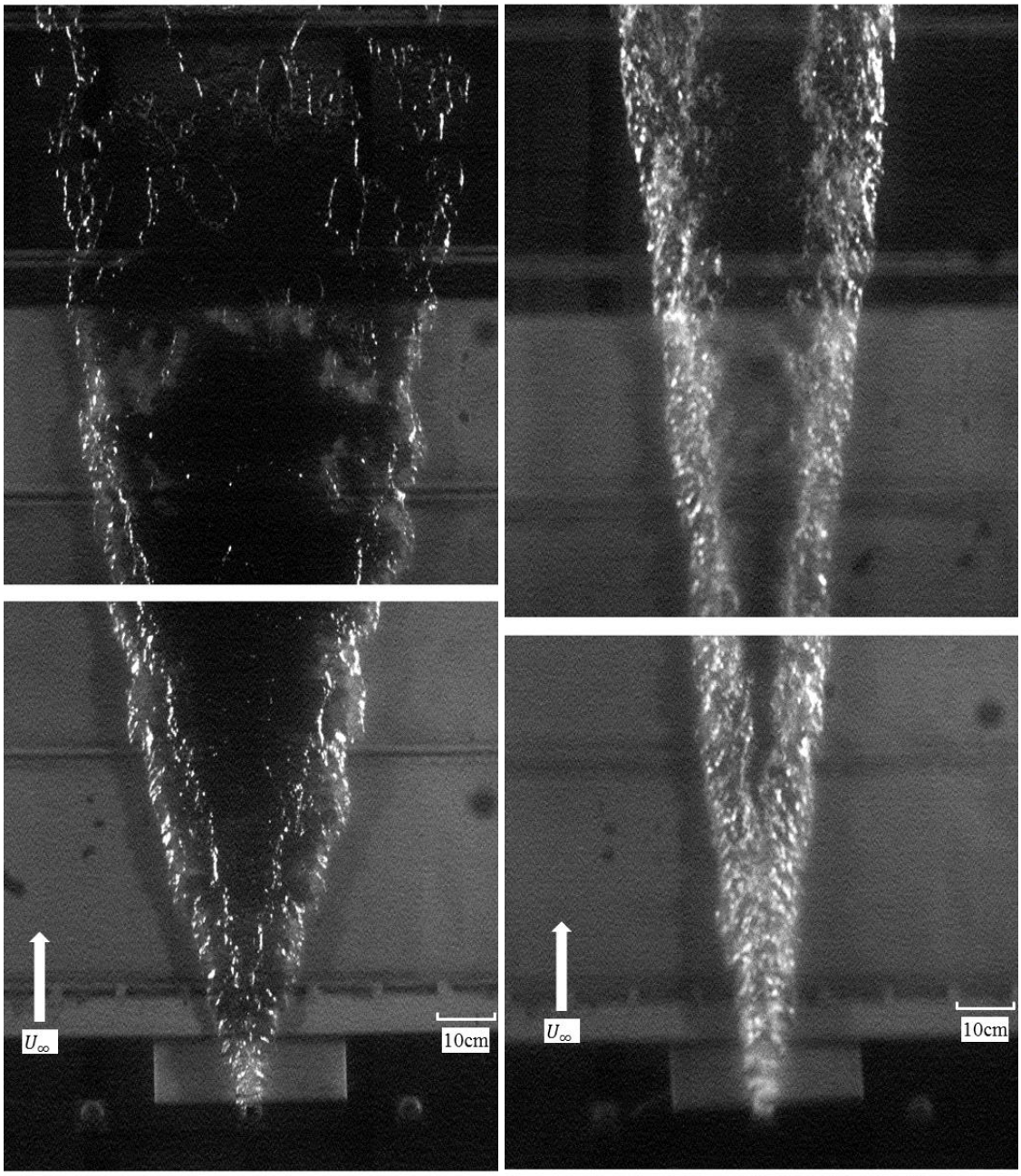

(a) (b)

Figure 6: A stitched image of Barge II with (a) a Delta type gas pocket (D_i ~ 20 mm, β = 90º, U_∞ = 2.0 ms^{-1}, Q_i = 4.3x10^{-3} m^{3}s^{-1}, δ = 53 mm) and of (b) a Lambda type gas pocket ($D_i \cong$ 10 mm, β = 90º, U_∞ = 4.0 ms^{-1}, Q_i = 6.7x10^{-3} m^{3}s^{-1}, δ = 53 mm).

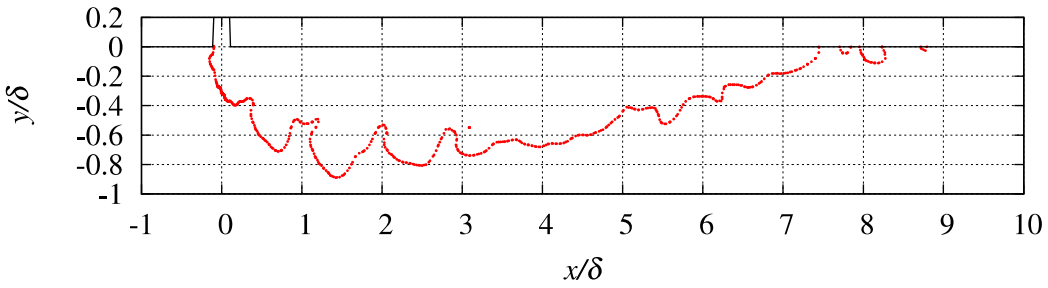

(a)

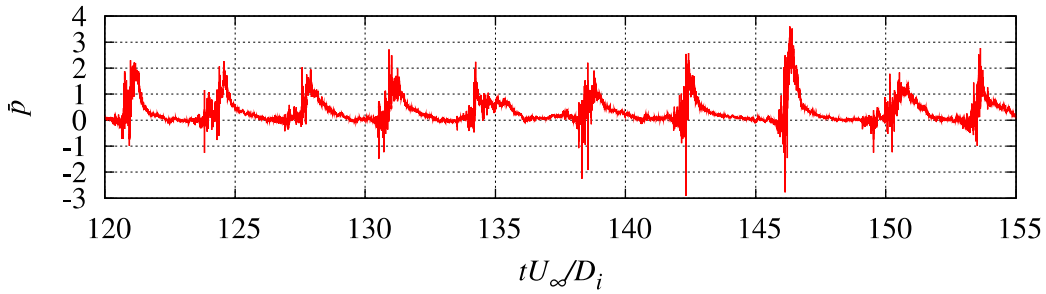

(b)

Figure 7: (a) instantaneous cavity profile and (b) time history of the normalized gas pressure $\bar{p}$ at the injector exit from the computation (Case A1). In reviewing (a) we should note that the gas exit pressure exceeds the static pressure in the boundary layer at jet penetration depth y/$\delta \cong$ -0.4, and the pressure fluctuations shown in (b) exhibits a frequency of St = 0.29.

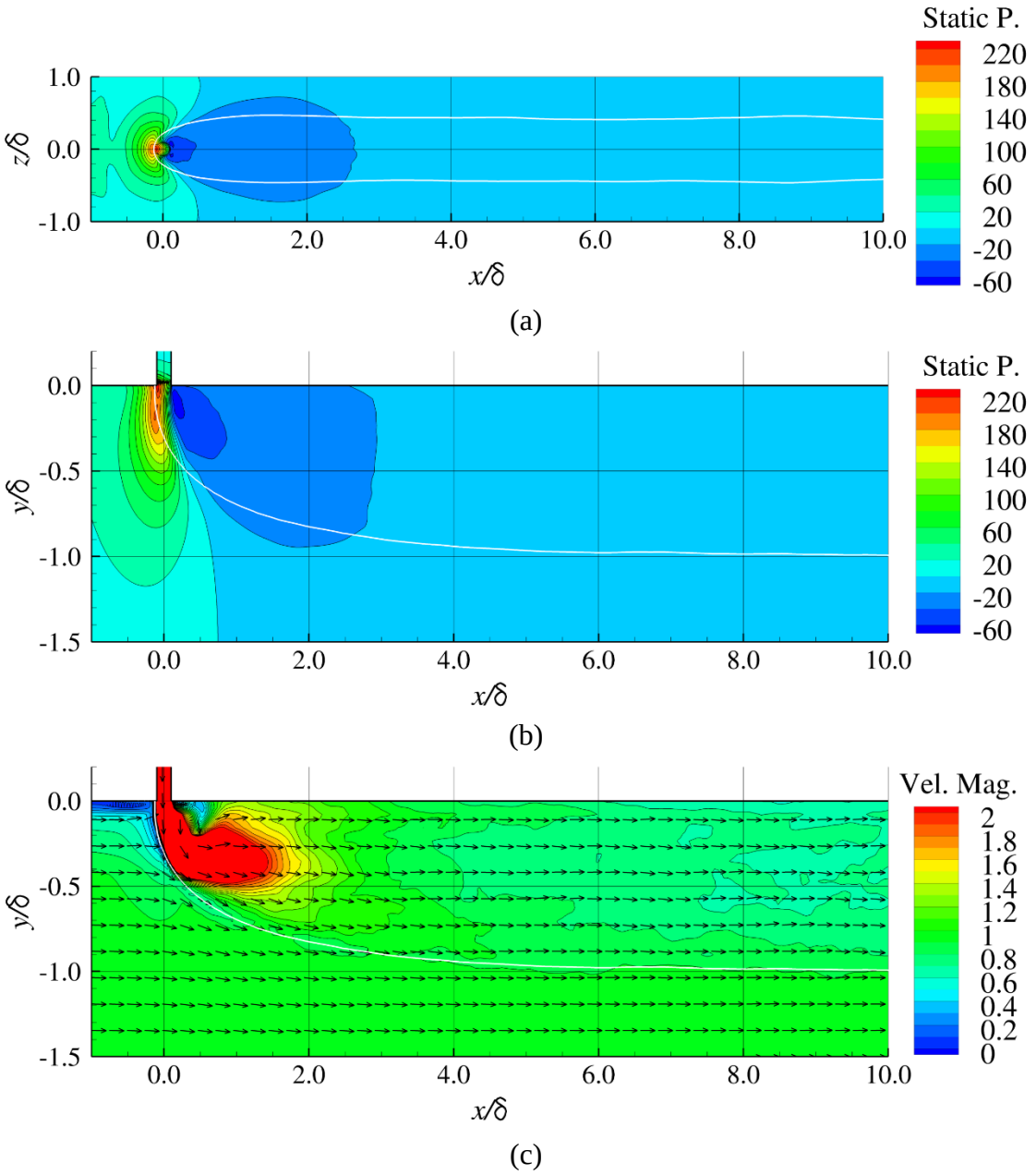

Figure 8: The computed time-averaged cavity flow *without* the effect of gravity (case A2); U_∞= 3.0 ms^{-1} and D_i = 10 mm, β = 90.0°, and Q_i= 5.0x10^{-3} m^{3}s^{-1}; δ= 51 mm; the static pressure on the flow boundary (a) and center-plane (b); the normalized velocity magnitude on the center plane (c) with non-scaled velocity vectors indicating direction The white line denotes the time-averaged cavity interface location.

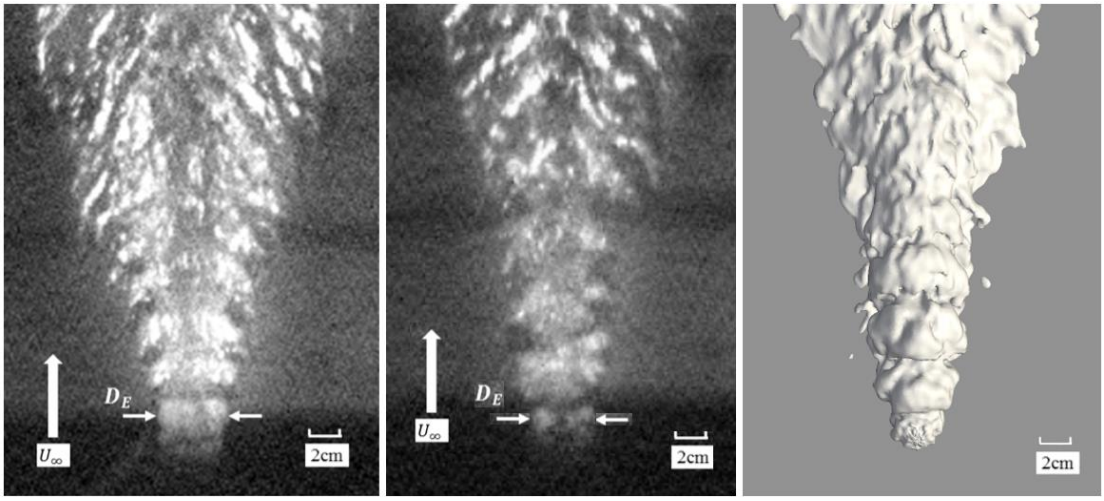

(a) (b) (c)

Figure 9: A close-up images of the gas jet showing the effective Diameter, D_E, and the puffing pattern observed during the present experiments: $D_i \cong 10$ mm, β, = 90º, $\delta \cong 52$ mm; (a) $U_\infty = 2.5$ ms^{-1}, $Q_i = 6.7\text{x}10^{-3}$ m^{3}s^{-1}; (b) $U_\infty = 3.0$ ms^{-1}, $Q_i = 5.0\text{x}10^{-3}$ m^{3}s^{-1}; and computation: (c) $U_\infty = 3.0$ ms^{-1}, $Q_i = 5.0\text{x}10^{-3}$ m^{3}s^{-1}

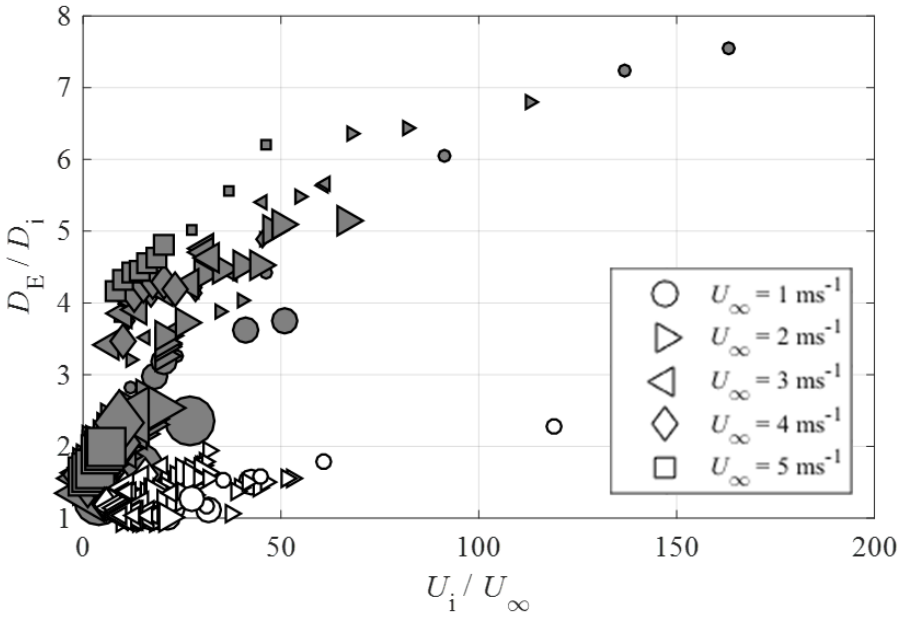

Figure 10: The effective jet exit diameter, D_E, as a function of velocity ratio. The different symbols denote various free-stream speeds, as indicated by the legend. The size of symbol indicates the orifice size, with largest corresponding to D_i = 20 mm, mid-size to D_i = 10 mm, and smallest to D_i = 5 mm. Empty markers represent data from Barge model I, with δ_1, and filled markers data from Barge model II, δ_2.

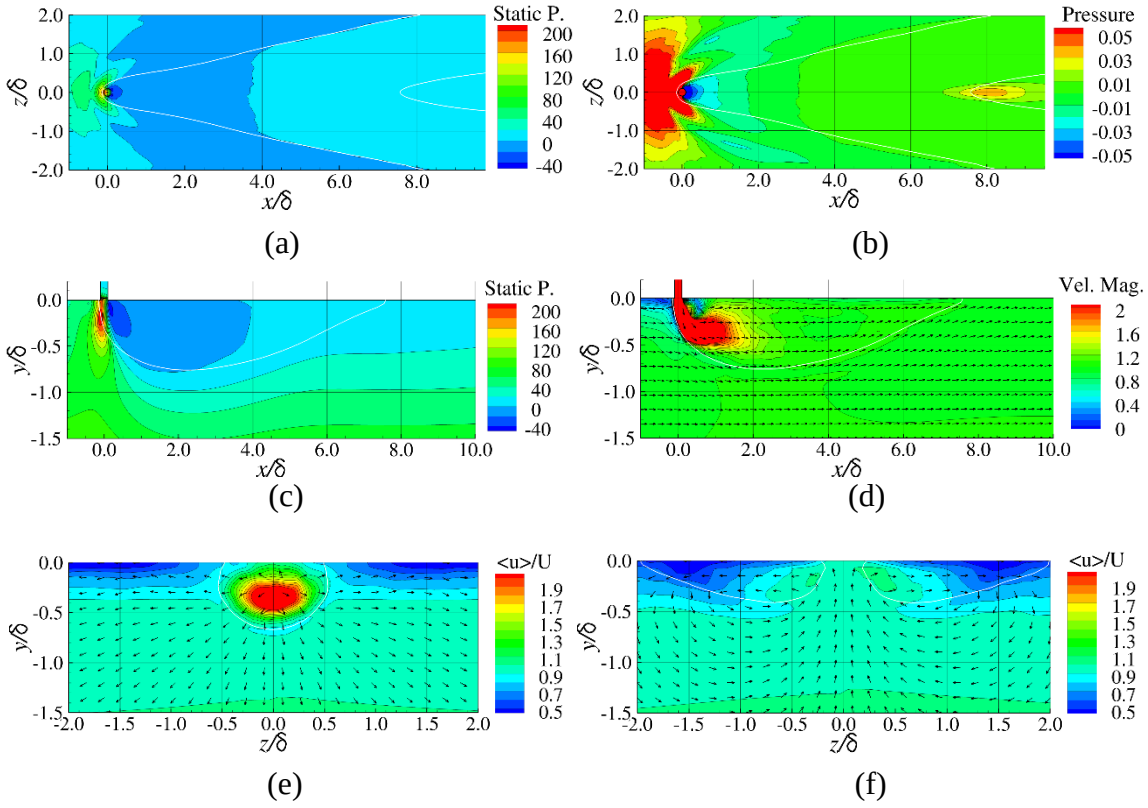

Figure 11: The computed time-averaged cavity flow *with* the effect of gravity (case A1); U_∞=3.0 ms^{-1} and D_i = 10 mm, β = 90.0°, and Q_i= 5.0x10^{-3} m^{3}s^{-1}; δ= 51 mm; (a) static pressure and (b) normalized pressure $\bar{p}$ on the flow boundary, and (c) static pressure on the x-y center-plane, and (d) velocity magnitude with non-scaled velocity vectors indicating direction. The velocity magnitude with non-scaled velocity vectors indicating direction on y-z plane at x/δ= 1 (e) and x/δ= 8 (f). The white line denoted the time-averaged cavity interface location.

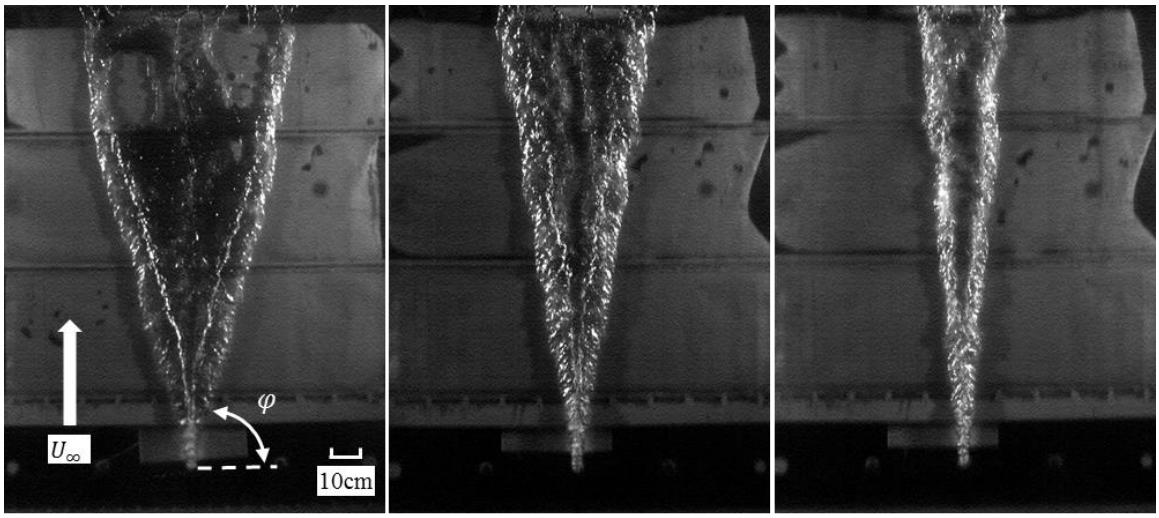

(a) (b) (c)

Figure 12: Images illustrating the change in sweep angle, φ, and chord length, C, with varying flow speed, U_∞, with fixed $D_i \cong 5$ mm, $\beta = 90^o$, and $Q_i = 2.0\text{x}10^{-3}$ m^3s^{-1}, for U_∞= 2.0 ms^{-1} (a), 3.0 ms^{-1} (b), and 4.0 ms^{-1} (c); $\delta \cong 52$ mm. The resulting sweep angles and chord lengths are (a) φ =74.2° and C = 64 mm, (b) φ =79.9°and C = 60 mm, (c) φ = 84.6° and C = 38 mm.

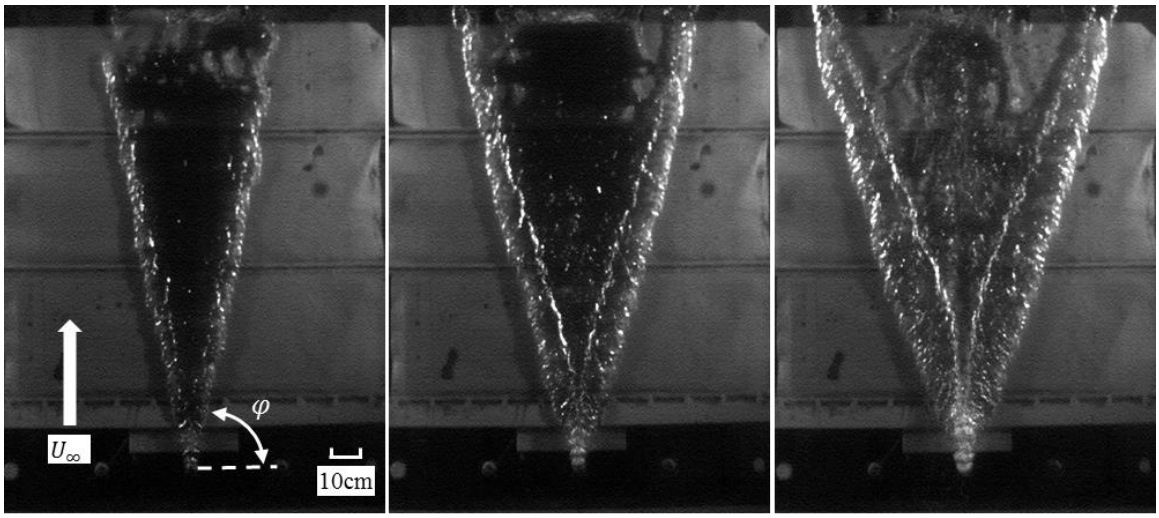

(a) (b) (c)

Figure 13: Images illustrating the change in sweep angle, φ, and chord length, C, with varying volume flow-rate, Q_i, with fixed $D_i \cong 10$ mm, $\beta = 90^o$, and $U_\infty = 2.0$ ms^{-1}, $\delta \cong 52$ mm, for $Q_i = 1.7\text{x}10^{-3}$ m^{3}s^{-1} (a), $3.3\text{x}10^{-3}$ m^{3}s^{-1} (b), and $6.5\text{x}10^{-3}$ m^{3}s^{-1}(c). The resulting sweep angles and chord lengths are (a) φ =76.7° and C = 44 mm; (b) φ =72.2°and C = 86 mm; (c) φ = 68.8° and C = 142 mm.

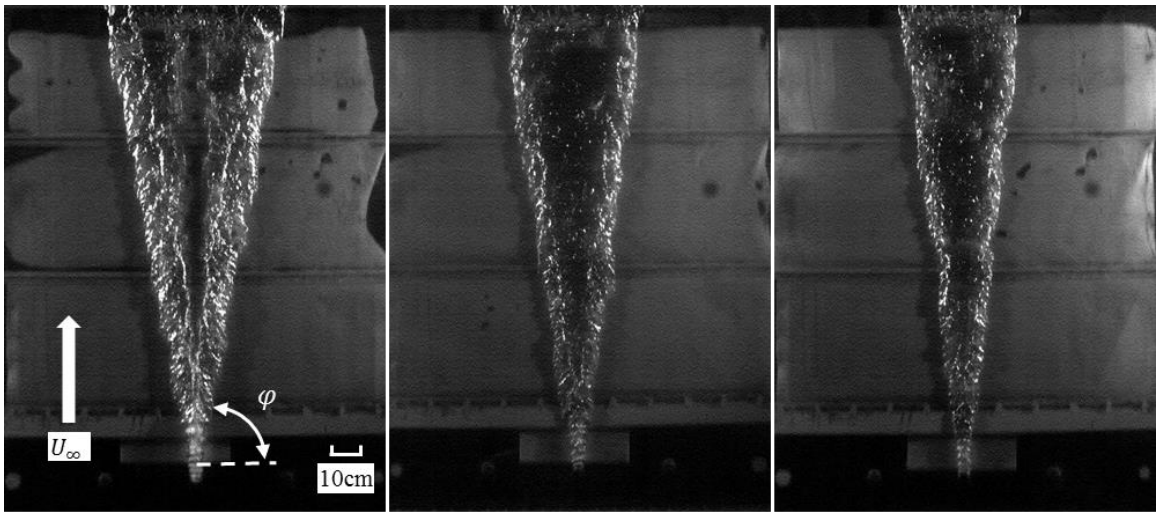

(a) (b) (c)

Figure 14: Images illustrating the change in sweep angle, φ, and chord length, C, with varying injection hole diameter D_i with fixed U_∞= 3 ms^{-1}, δ = 51mm, β = 90.0°, and Q_i = 2.5x10^{-3} m^{3}s^{-1}, for D_i = 5 mm (a), 10 mm (b), and 20 mm (c). The resulting sweep angles and chord lengths are (a) φ = 79.7 ° and C = 90 mm; (b) φ = 81.8 °and C = 66 mm; (c) φ = 82.4 ° and C = 40 mm.

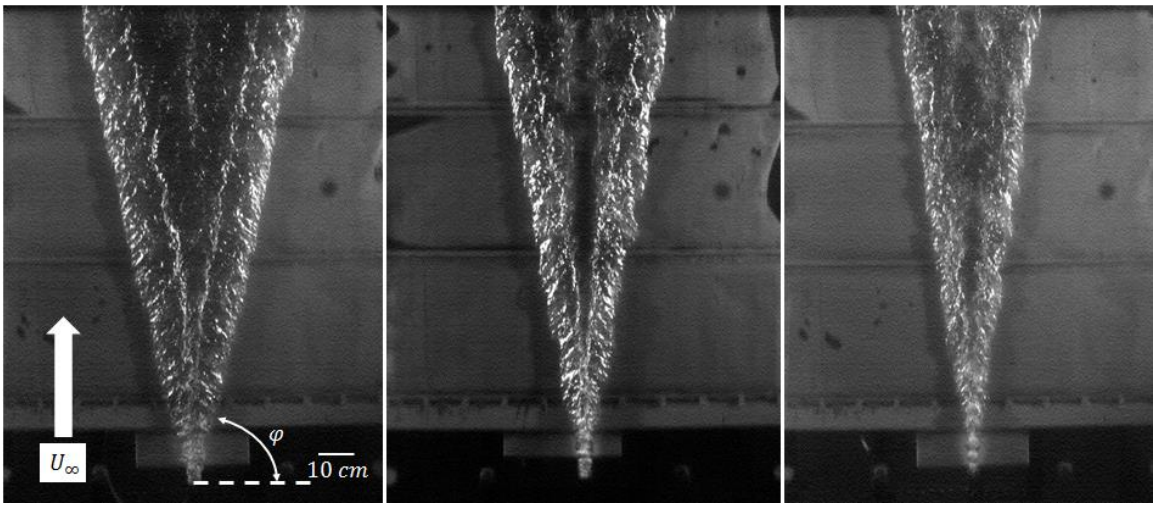

(a) (b) (c)

Figure 15: Images illustrating the change in sweep angle, φ, and chord length, C, with varying injection angle, β, with fixed $D_i \cong 5$ mm, $U_\infty = 3.0$ ms^{-1}, $\delta = 53$ mm, and $Q_i = 2.5\text{x}10^{-3}$ m^{3}s^{-1} for $\beta = 157.5°$ (a), 90.0° (b), 22.5° (c). The resulting sweep angles and chord lengths are (b) $\varphi = 76.0°$ and $C = 113$ mm; (b) $\varphi = 79.7°$ and $C = 90$ mm; (c) $\varphi = 81.2°$ and $C = 63$ mm.

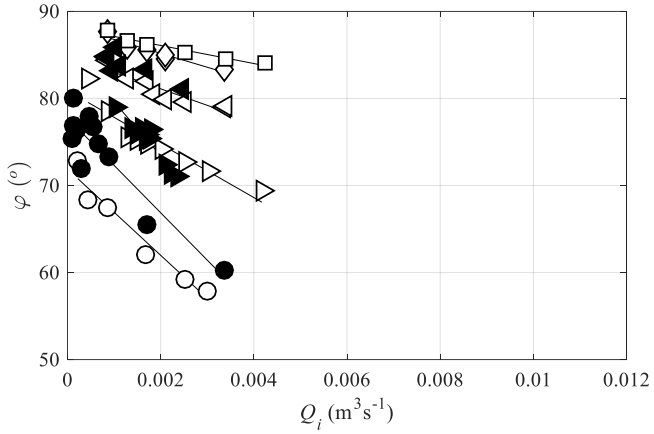

(a)

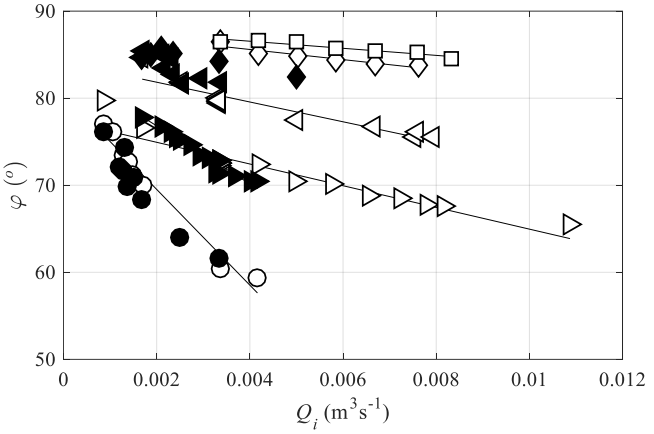

(b)

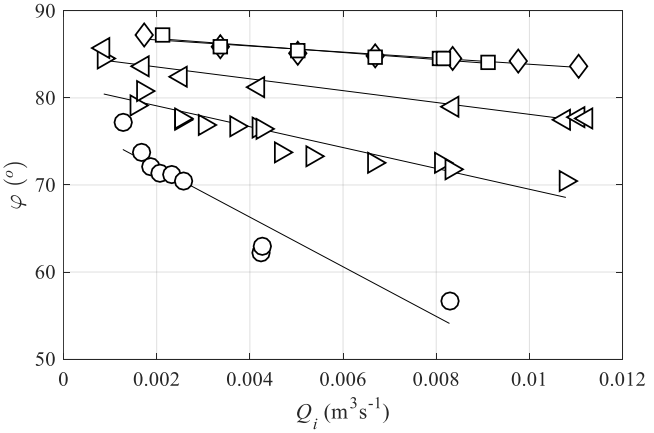

(c)

Figure 16: Sweep angle, φ, *versus* volume flow-rate, Q_i, for varying flow speeds, β = 90º: $D_i \cong$ 5 mm (a), $\cong$ 10 mm (b), and $\cong$ 20 mm (c). Markers are such that U_∞= 1.0 ms^{-1} (○), 2.0 ms^{-1} (▷), 3.0 ms^{-1} (◁), 4.0 ms^{-1} (◇), and 5.0 ms^{-1} (□). Filled markers represent data from Barge model I, with δ_1, and empty markers data from Barge model II, δ_2.

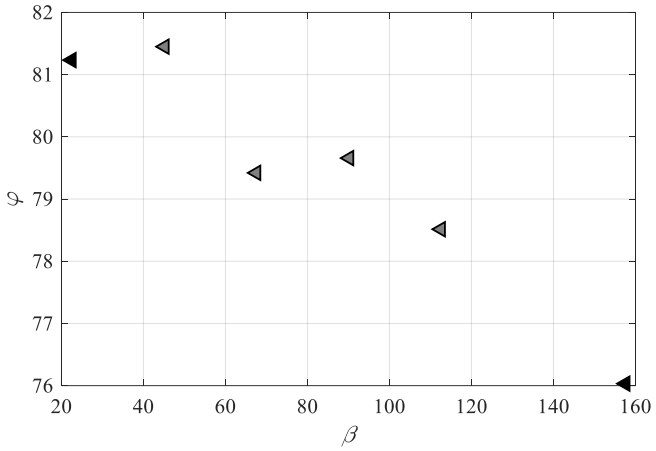

Figure 17: Sweep angle, φ, *versus* injection angle, β, for U_∞= 3.0 ms^{-1}, Q_i = 2.5x10^{-3} m^{3}s^{-1} and for D_i = 5 mm. The open symbols signify Lambda, grey Transitional and black filled a Delta-topology. Note: for the particular example data shown, Lambda-topology (open symbols) was not observed.

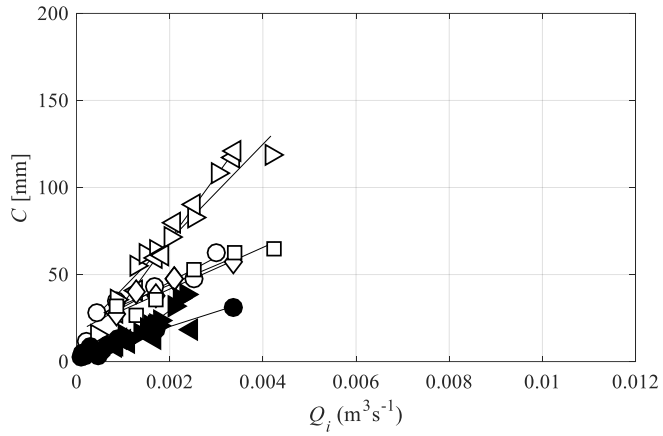

(a)

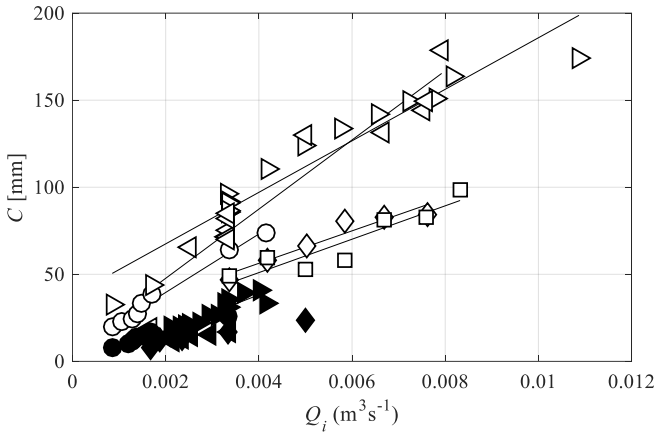

(b)

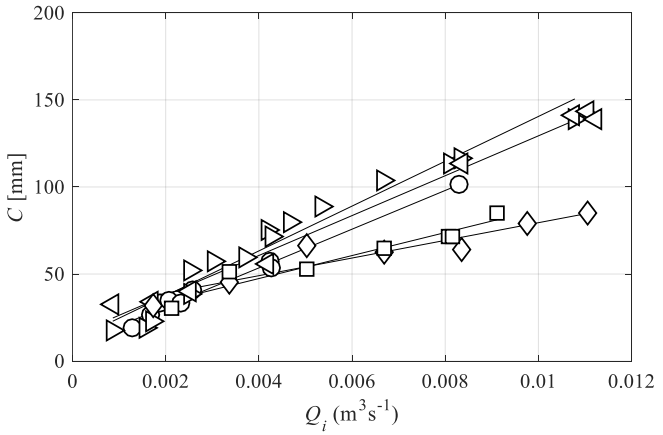

(c)

Figure 18: Chord length, C, *versus* volume flow-rate, Q_i, for varying flow speeds, β = 90^o: $D_i \cong$ 5 mm (a), $\cong$ 10 mm (b), and $\cong$ 20 mm (c). Symbols are same as in Figure 16.

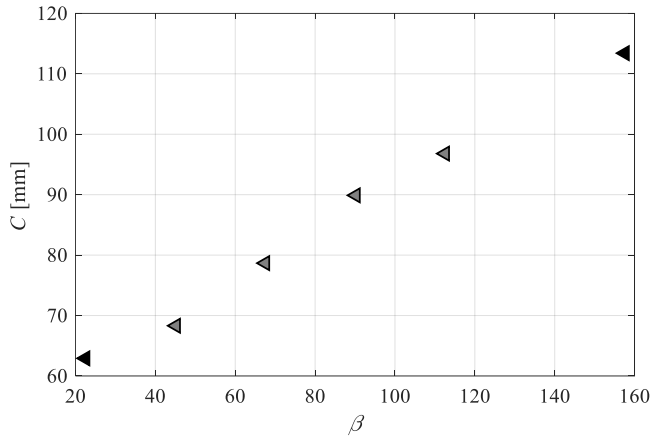

Figure 19: Chord length, C, *versus* injection angle, β, for U_∞= 3.0 ms^{-1}, Q_i = 2.5x10^{-3} m^{3}s^{-1} and for D_i = 5 mm. The open symbols signify Lambda, grey Transitional and black filled a Delta-topology. Note: for the particular example data shown, Lambda-topology (open symbols) was not observed.

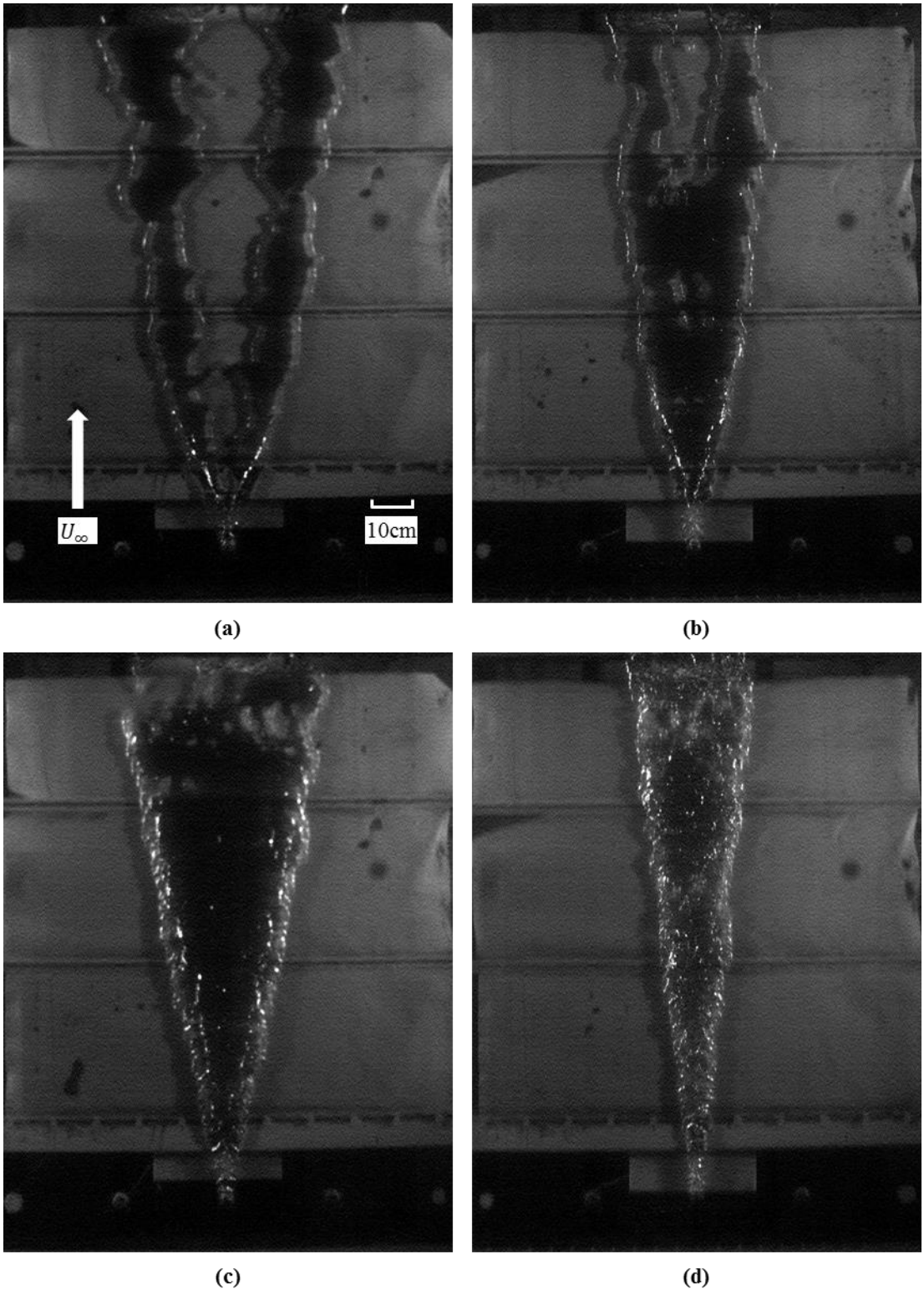

Figure 20: The topologies of the gas jet for low and higher speed cross-flow; the speed varies from U_∞ = 1.0, 1.5, 2.0, and 3.0 ms^{-1} (a – d) and 51 mm < δ < 57 mm the other conditions are fixed at D_i ~ 10 mm, Q_i = 1.7x10^{-3} m^3s^{-1}, and β = 90.0°.

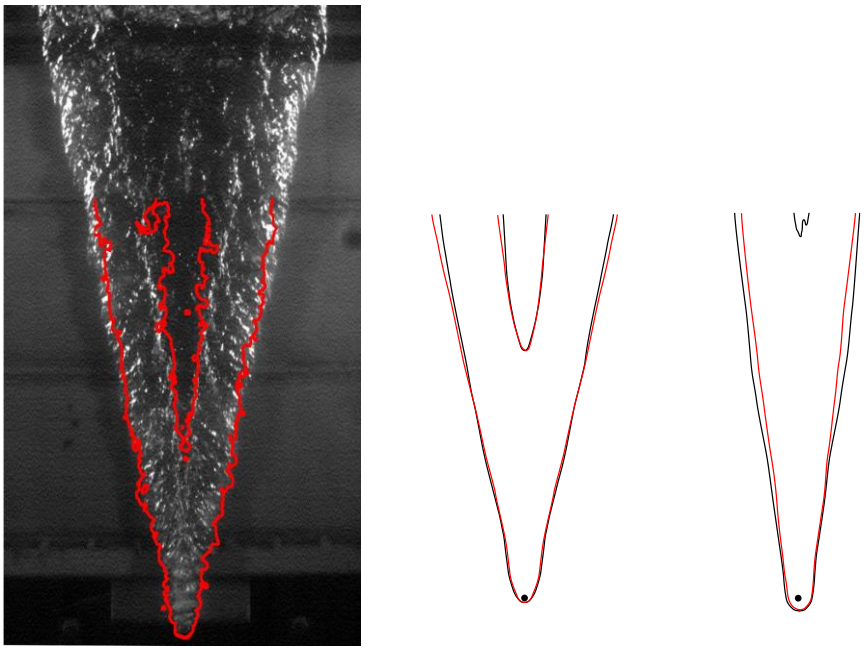

(a) (b) (c)

Figure 21: (a) A comparison of the instantaneous computed and observed plan view of the cavity topology for Case A1 (see Table 3). Comparison of the time-averaged computed cavity topologies (solid black lines) and the approximate experimental cavity topologies (solid red lines) for Case A1 (b) and D (c).

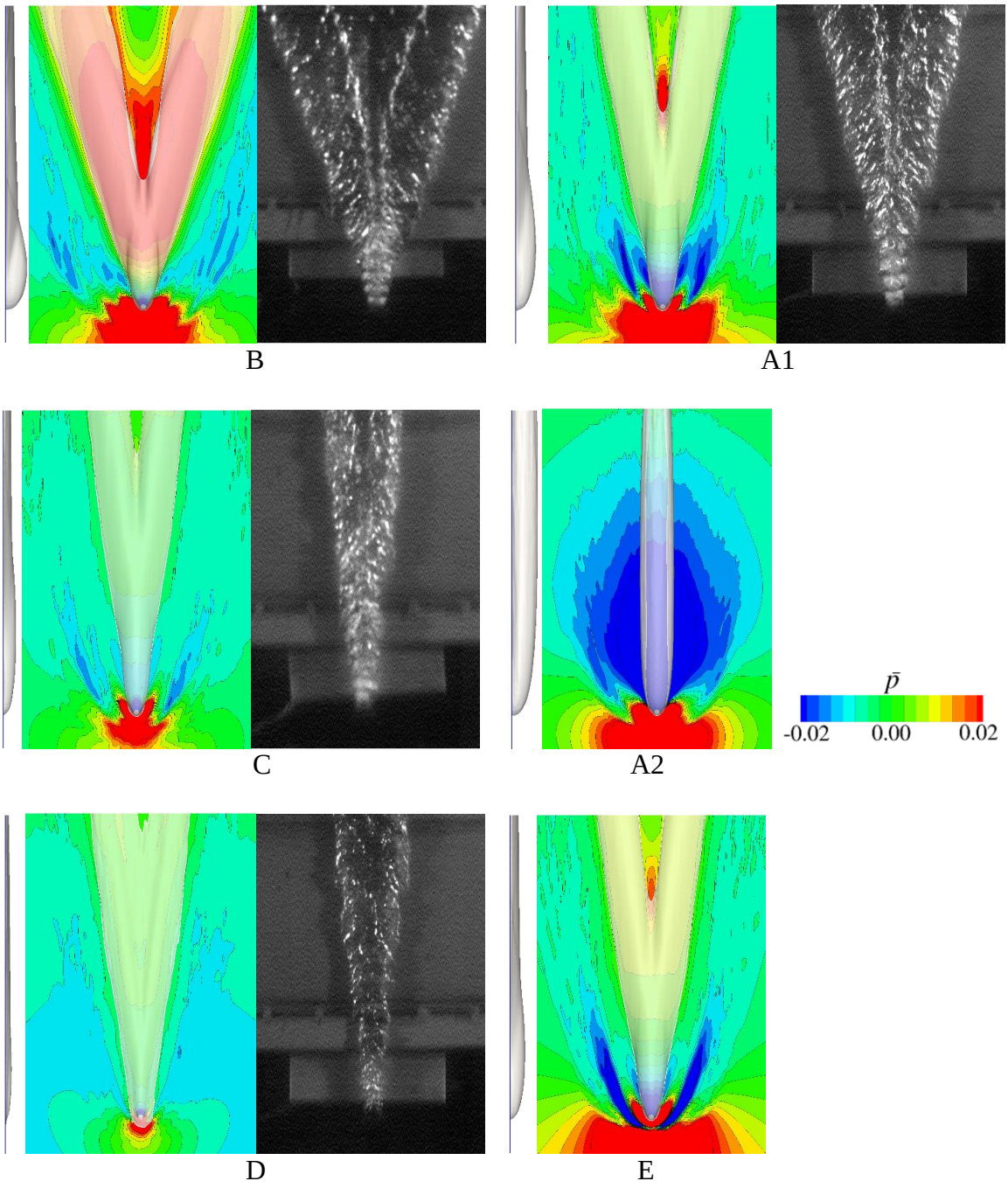

Figure 22: Profile and plan views of the computed cavity topologies and contours of the normalized pressure $\bar{p}$ on the flow boundary for cases listed in Table 3. Comparison figure from experiment include, if available. All the plan views show approximately a 46 by 68 cm region.

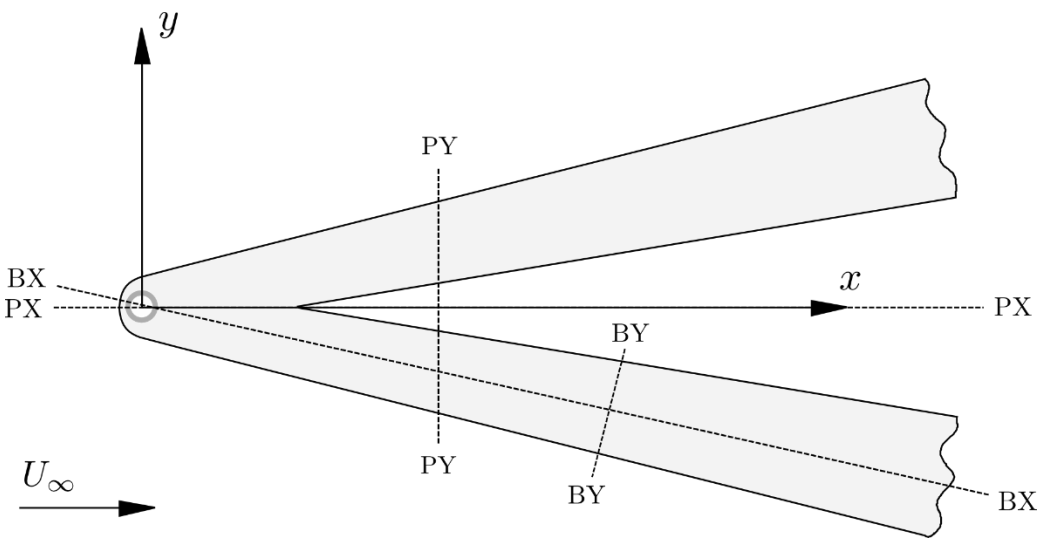

Figure 23: Illustration of the branch-aligned coordinate system. Section PX is the plane of symmetry parallel to the mean flow direction; Sections PY are the planes perpendicular to the surface and the mean flow direction; Section BX is the plane parallel to and centered on the gas branch; and Sections BY are planes normal the gas branch.

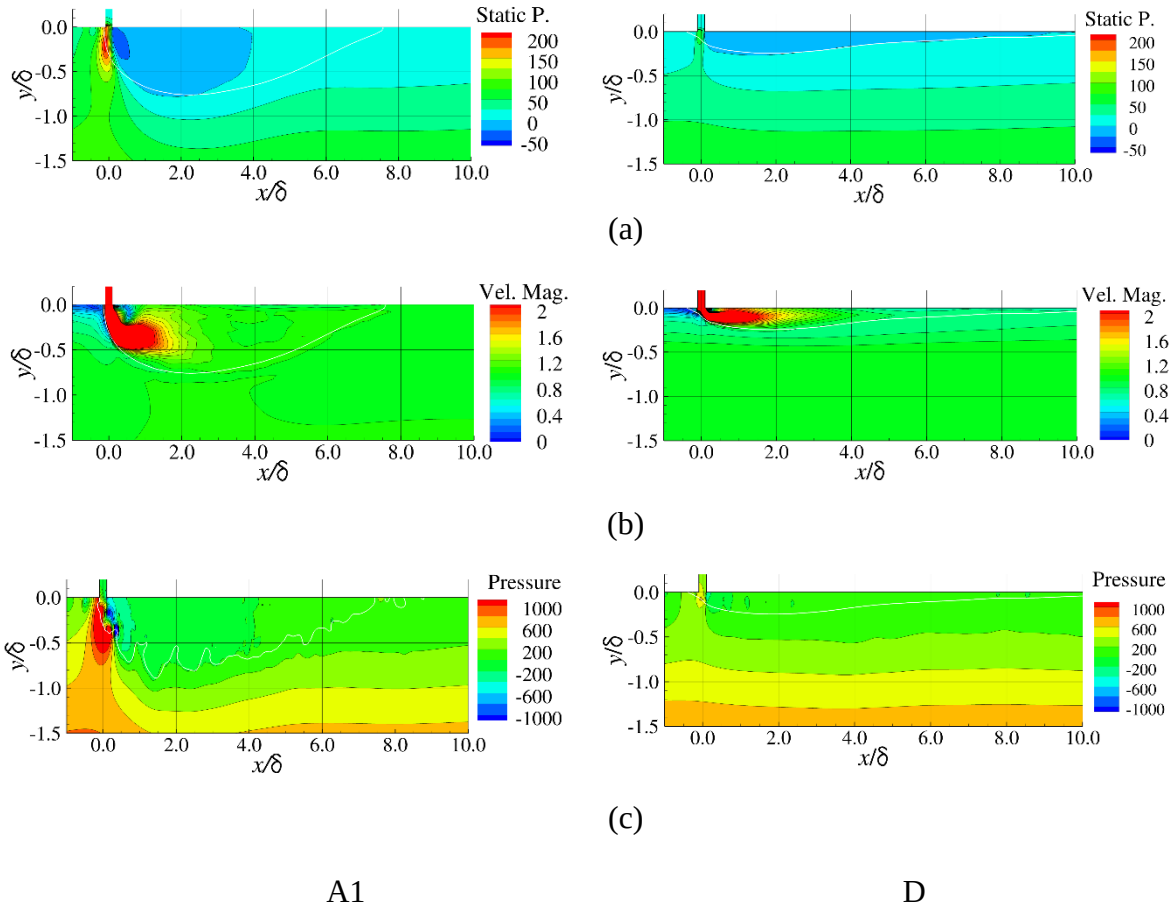

Figures 24: The time-averaged (a) static pressure, p, and (b) the velocity magnitude, $|\boldsymbol{u}|/U_\infty$, on the PX plane for cases A1 (Q_i = 5.0x10^{-3} m^{3}s^{-1}) and D (Q_i = 1.7x10^{-3} m^{3}s^{-1}); (c) is an instantaneous realization of the pressure field $\bar{p}$. The solid line indicates the gas-liquid interface defined for 50% void fraction.

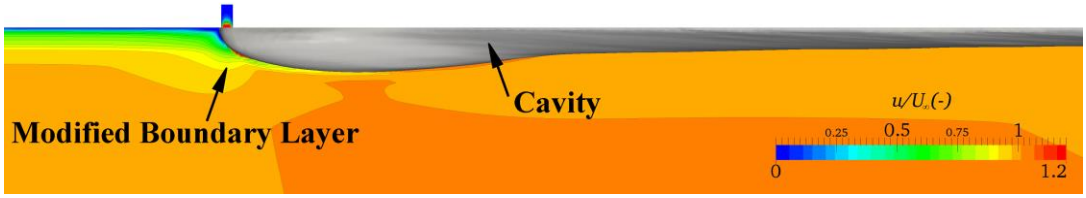

(a)

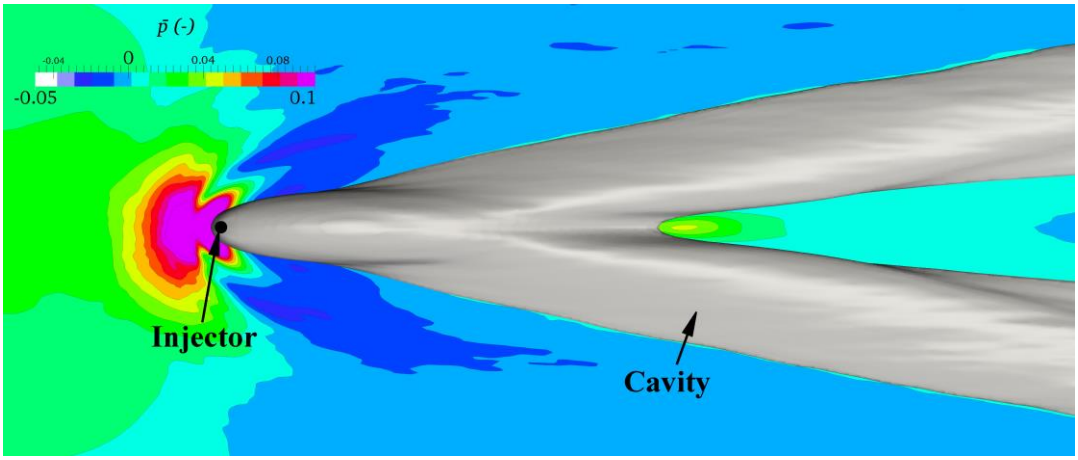

(b)

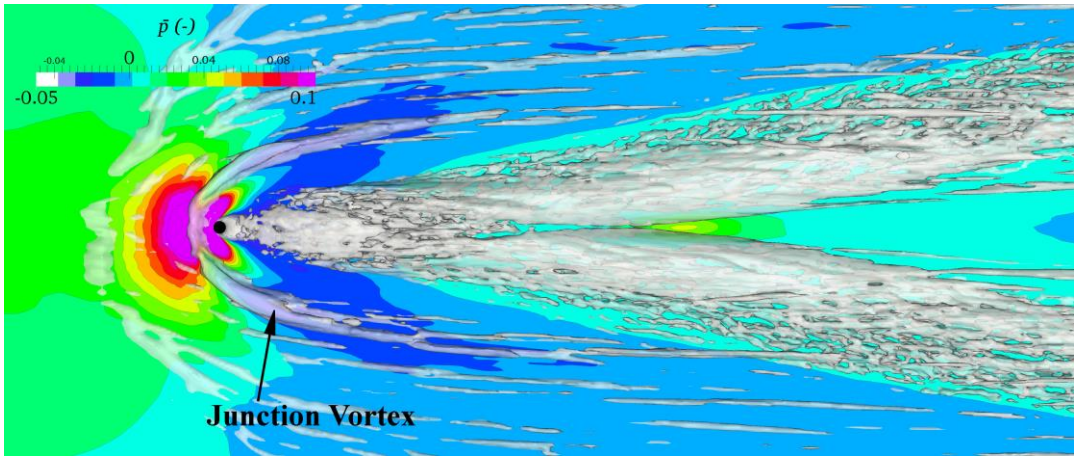

(c)

Figure 25: Case A1 (a) velocity magnitude, $|\boldsymbol{u}|/U_\infty$, on the centerplane, and the cavity (defined as 50% time-averaged void fraction) are shown as the dark gray iso-surface (b) The time-averaged normalized pressure, $\overline{p}$, on the top boundary and the cavity, (c) The time-averaged normalized pressure, $\overline{p}$, on the top boundary, and an iso-surface of the Q-criterion (Q = 10) illustrating the junction vortex formed in front of the gas branches.

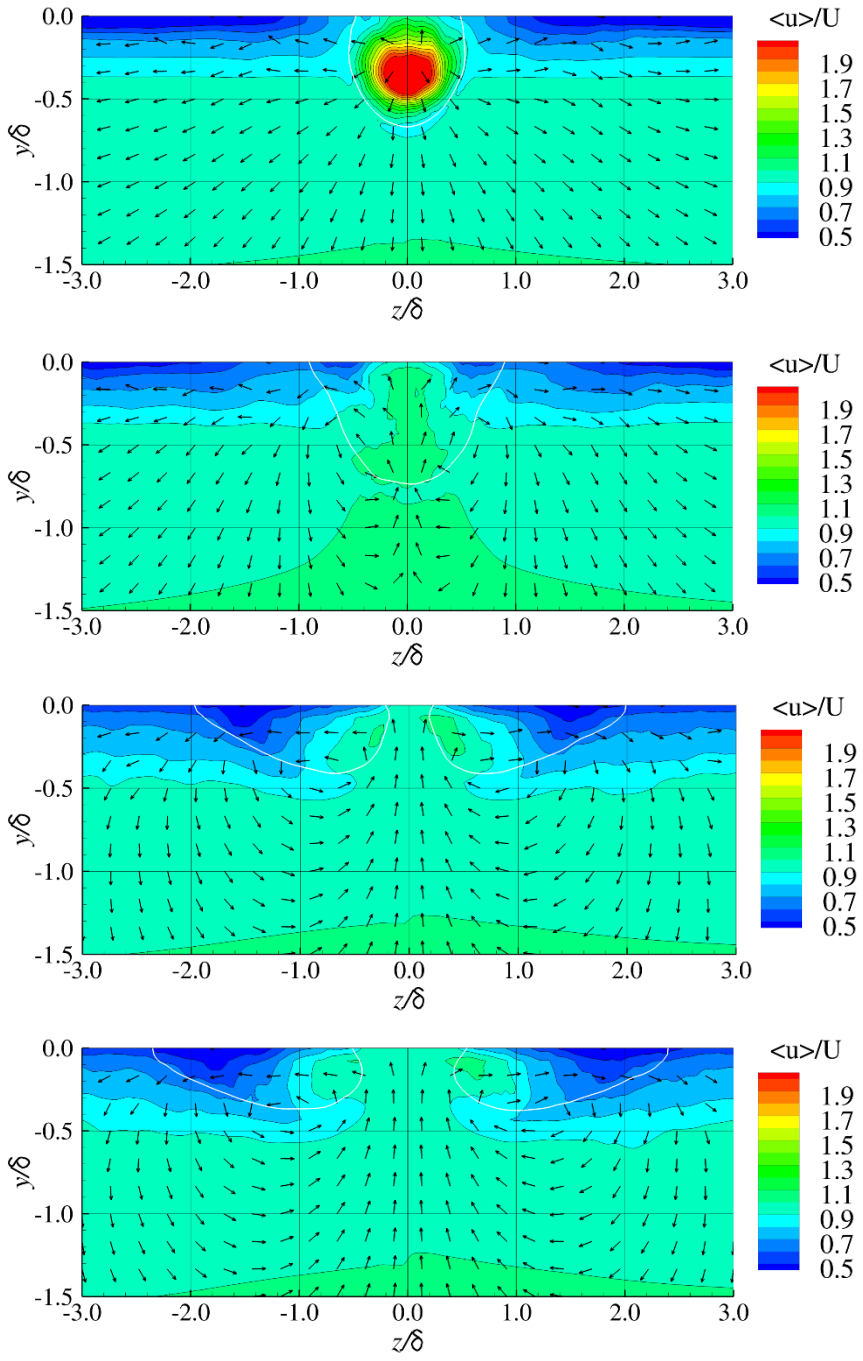

Figures 26: A series PY planes presenting the time-averaged in-plane velocity magnitude, for the case A1. The solid line indicates the gas-liquid interface defined for 50% void fraction. The cases are for x/δ = 1, 3, 8, 10.

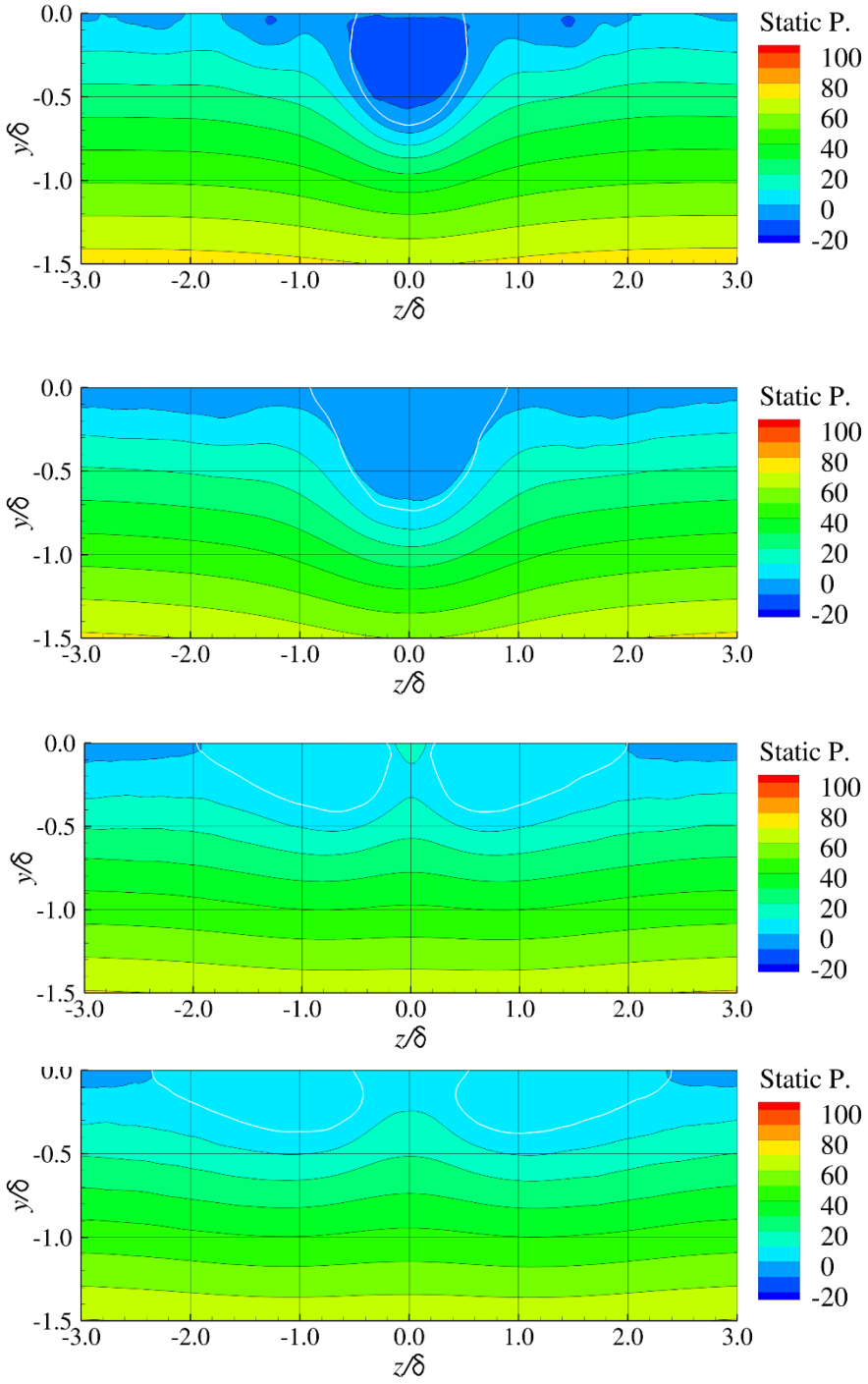

Figure 27: The static pressure, p, on a series of planes PY planes for case A1. The solid line indicates the gas-liquid interface defined for 50% void fraction. The cases are for x/δ = 1, 3, 8, 10.

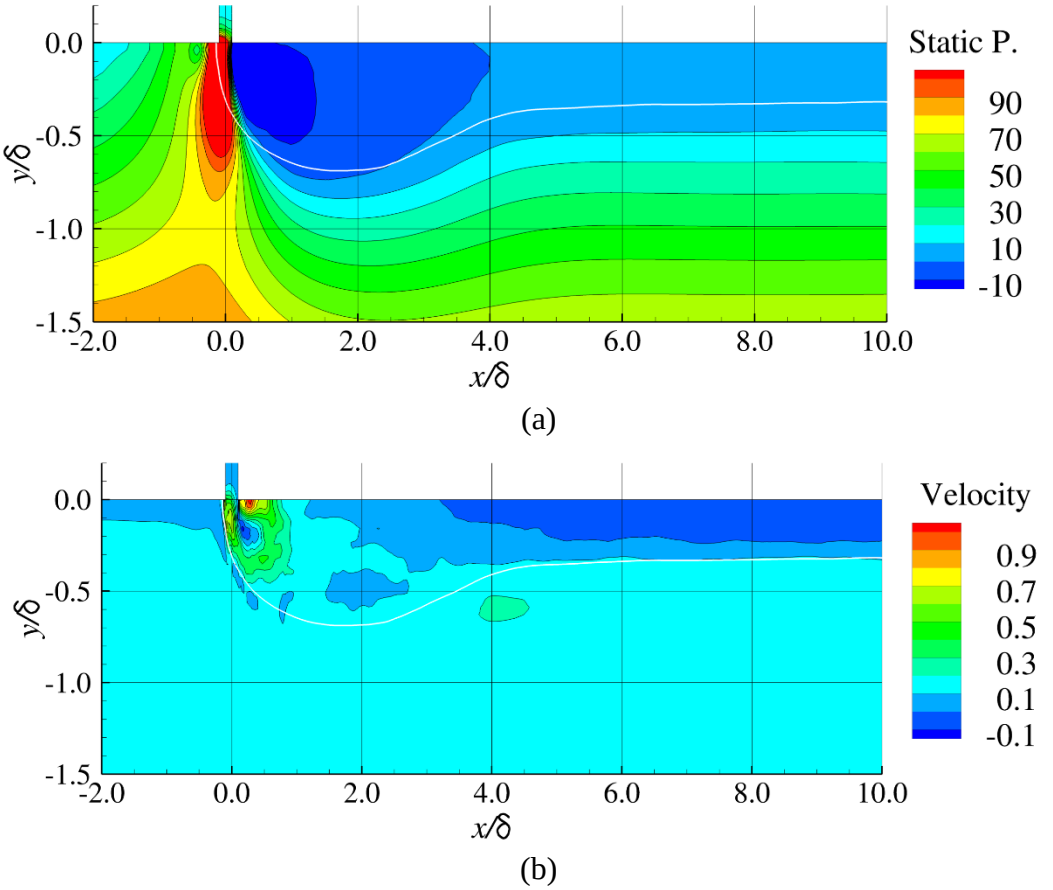

Figure 28: The (a) static pressure, p, and (b) the in-plane velocity magnitude, $|\boldsymbol{u}|/U_{\infty}$, for the flow along on gas branch on the plane BX for the case A1. The solid white line indicates the gas-liquid interface as 50% time-averaged void fraction.

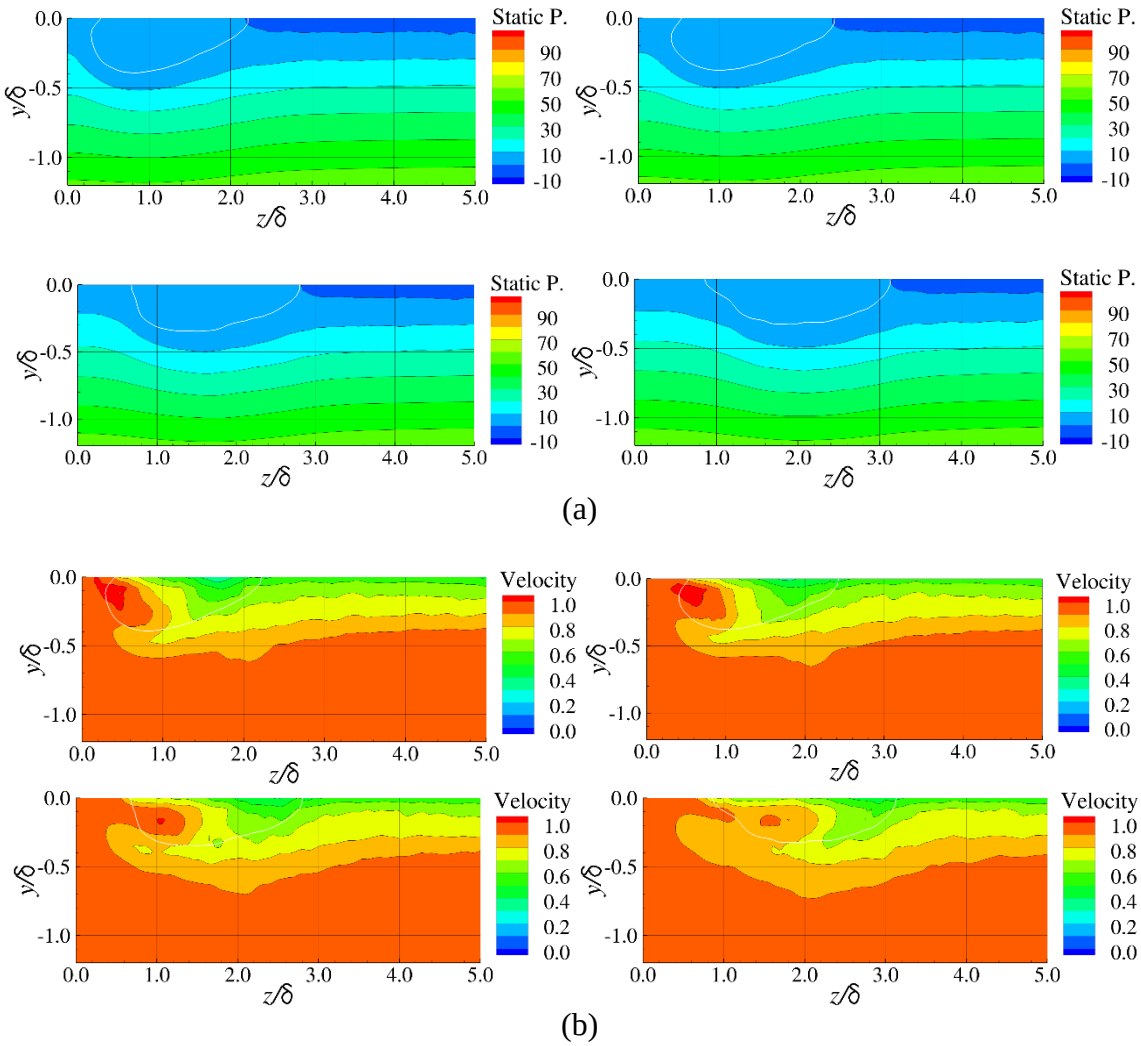

Figure 29: The (a) static pressure, p, and (b) the in-plane velocity magnitude, for the flow in the plane BY for the case A1. The solid line indicates the gas-liquid interface defined for 50% void fraction. The planes are at x'/δ = 9, 10, 12, 14

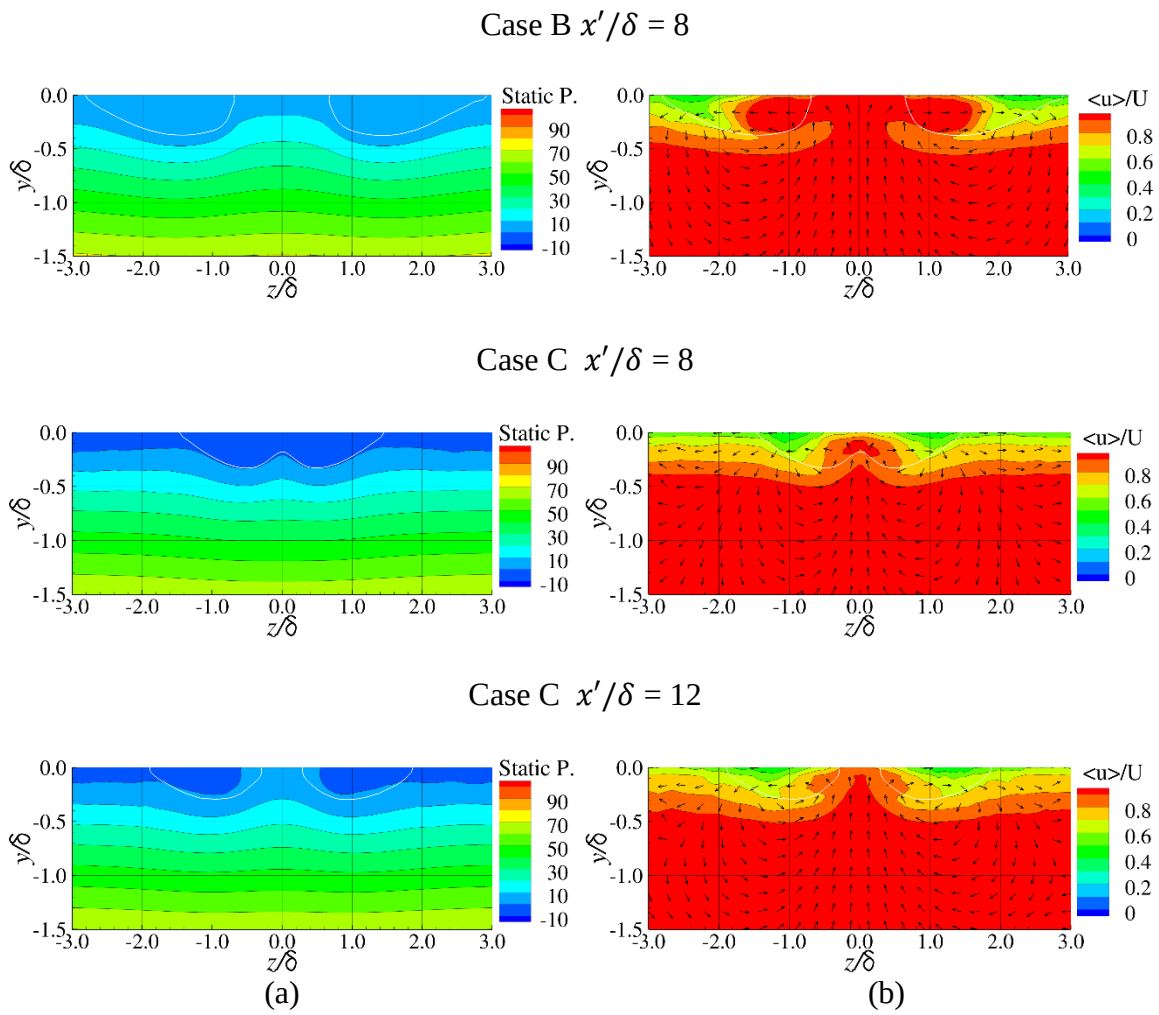

Figures 30: The (a) static pressure, p, (b) flow speed and velocity vectors for the cases B and C. Case B is for U_∞= 2 ms^{-1} and x'/δ = 8, and Case C is for U_∞= 4 ms^{-1} and x'/δ = 8 or 12. The solid line indicates the gas-liquid interface defined for 50% void fraction.

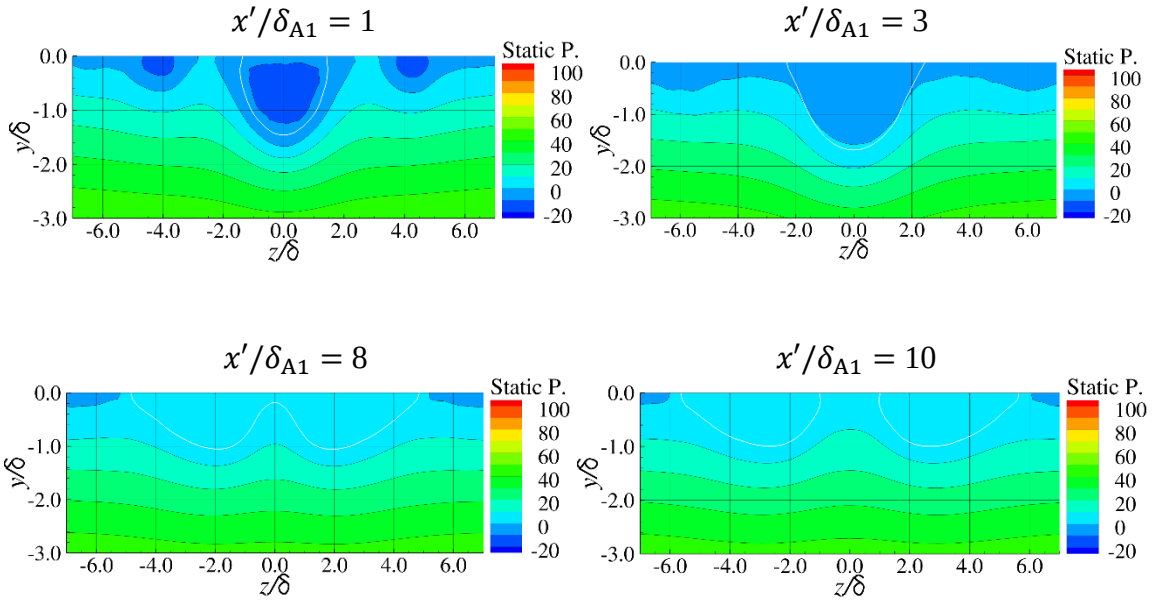

(a)

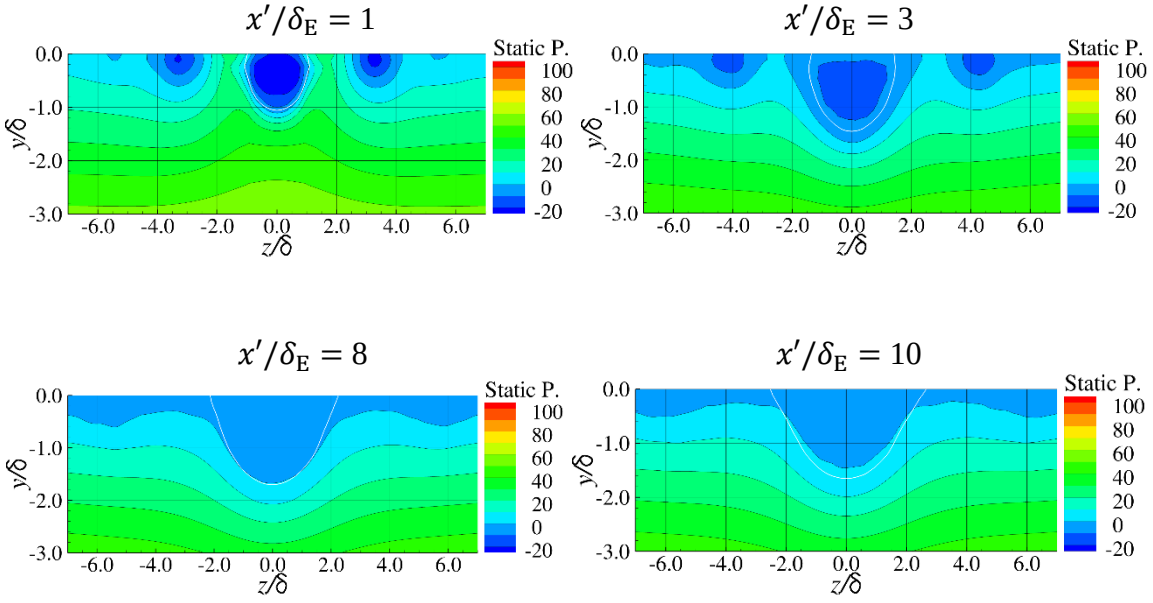

(b)

Figures 31: The time-averaged static pressure, p case E at (a) x'/δ_{A1} = 1, 3, 8, 10, and (b) $x'/\delta_{E} = 1$, 3 ,8, 10, respectively. The boundary layer for Case E is 1/3 that of Case A1. The solid line indicates the gas-liquid interface defined for 50% void fraction.

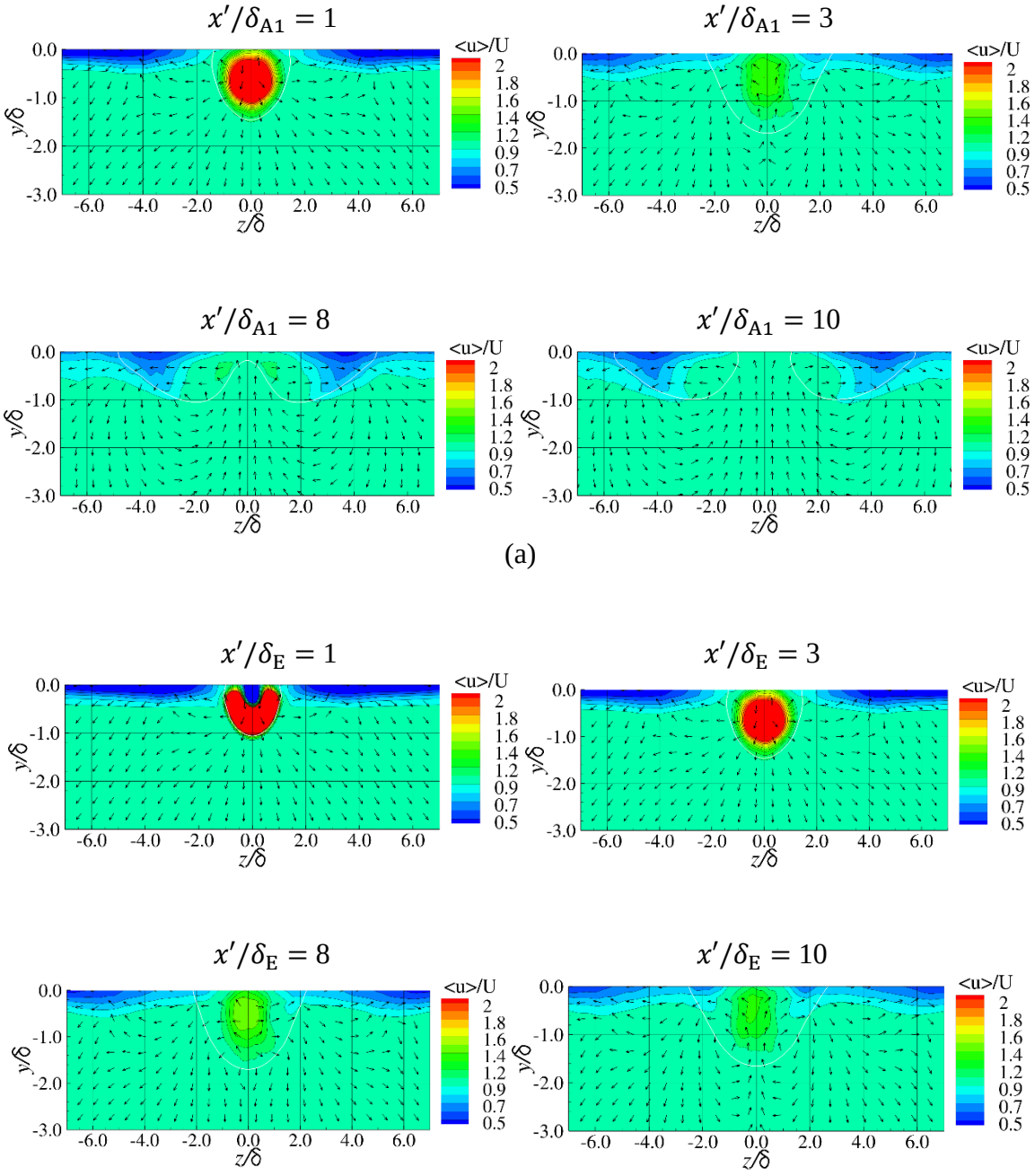

Figure 32: The time-averaged flow speed and velocity vectors for case E at (a) x'/δ_{A1} = 1, 3, 8, 10, and (b) $x'/\delta_E = 1, 3, 8, 10$, respectively. The boundary layer for Case E is 1/3 that of Case A1. The solid line indicates the gas-liquid interface defined for 50% void fraction.

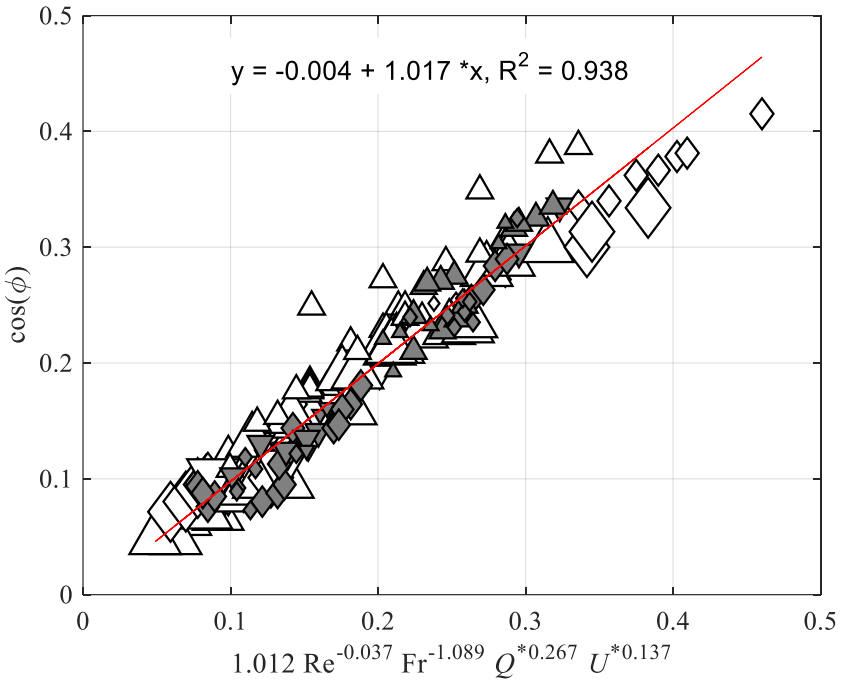

Figure 33: A plot of cosφ *versus* a power-law employing the Froude number, Fr $= U_\infty/\sqrt{g\delta}$, the Reynolds number, Re $= U_\infty\delta/\nu_\infty$, the scaled gas injection flowrate, $Q^* = Q_i/U_\infty\delta^2$, and the injection speed ratio, $U^* = U_i/U_\infty$, for $U_\infty \geq 2$ ms^{-1} and wall-normal injection ($\beta = 90^o$); the markers represent Delta (△), Transition (◇), and Lambda (▽) cavities; Filled markers represent data from Barge model I, with δ_1, and empty markers represent data from Barge model II, δ_2; and the size of the marker represents the orifice size, *e.g.* (▵) D_i ~ 5 mm, (△) D_i ~ 10 mm, (△) D_i ~ 20 mm.

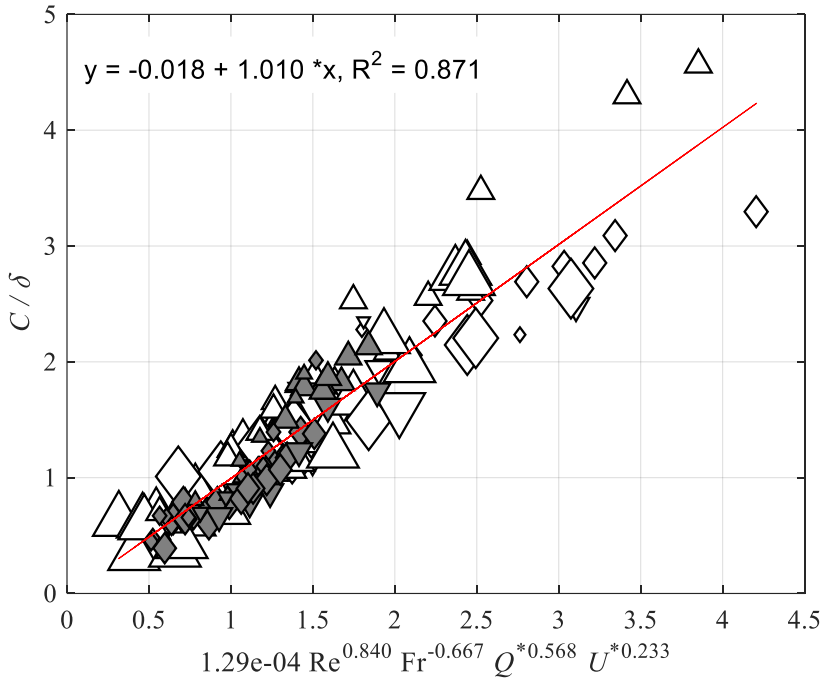

Figure 34: A plot of C/δ *versus* a power law employing the Froude number, $\mathrm{Fr} = U_\infty/\sqrt{g\delta}$, the Reynolds number, $\mathrm{Re} = U_\infty\delta/\nu_\infty$, the scaled gas injection flowrate, $Q^* = Q_i/U_\infty\delta^2$, and the injection speed ratio, $U^* = U_i/U_\infty$, for $U_\infty \geq 2$ ms^{-1} and wall-normal injection ($\beta = 90^o$); the markers represent Delta (△), Transition (◇), and Lambda (▽) cavities; Filled markers represent data from Barge model I, with δ_1, and empty markers represent data from Barge model II, δ_2; and the size of the marker represents the orifice size, *e.g.* (▵) D_i ~ 5 mm, (△) D_i ~ 10 mm, (△) D_i ~ 20 mm.

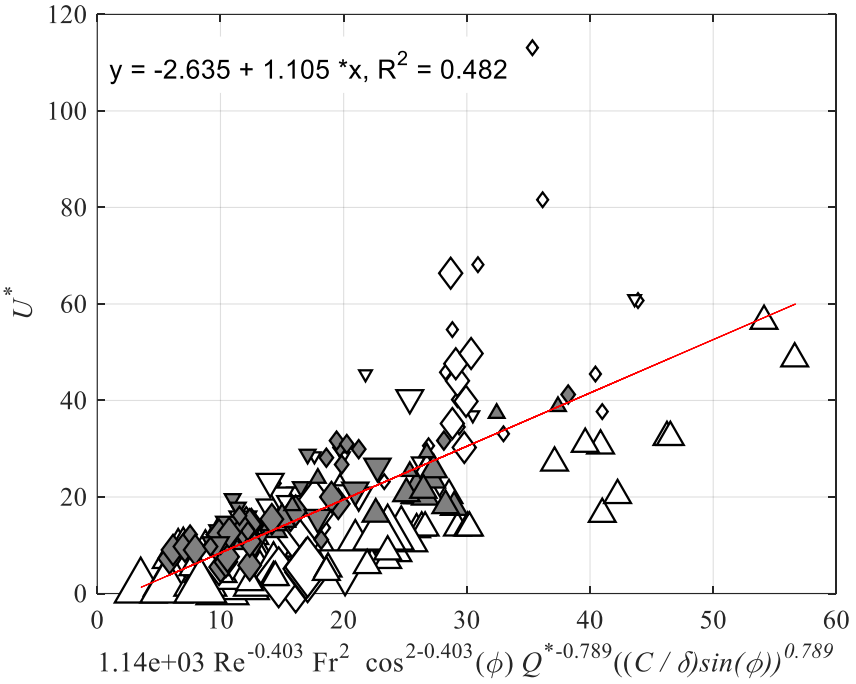

Figure 35: A plot of $\mathrm{Re}^{-\hat{m}}\,\mathrm{Fr}^2\cos^{2-\hat{m}}\varphi\;Q^{*\hat{p}}(\sin\varphi)^{-\hat{p}}$ *versus* U^* for $U_\infty \geq 2$ ms^{-1} and wall-normal injection ($\beta = 90^o$); and the data shows the best linear fit for $\hat{m} = 0.40$ and $\hat{p} = -0.79$ with a linear correlation is 0.48; the markers represent Delta (△), Transition (◇), and Lambda (▽) cavities; Filled markers represent data from Barge model I, with δ_1, and empty markers represent data from Barge model II, δ_2; and the size of the marker represents the orifice size, *e.g.* (▵) D_i ~ 5 mm, (△) D_i ~ 10 mm, (△) D_i ~ 20 mm.

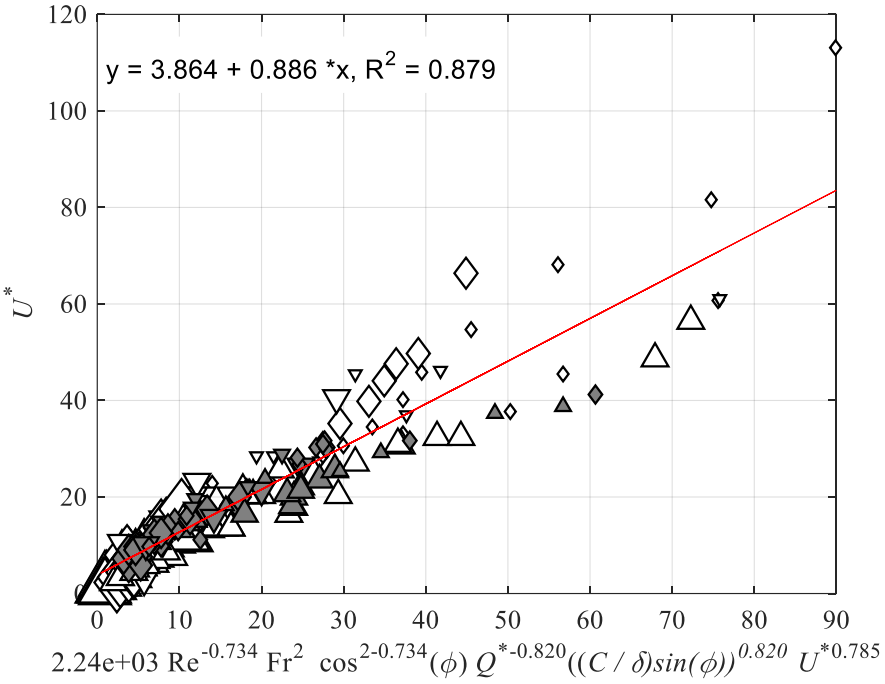

Figure 36: A plot of $\mathrm{Re}^{-\hat{m}}\,\mathrm{Fr}^2\cos^{2-\hat{m}}\varphi\,Q^{*\hat{p}}\left(\frac{C}{\delta}\sin\varphi\right)^{-\hat{p}}\,U^{*\hat{q}}$ *versus* U^* for $U_\infty \geq 2$ ms^{-1} and wall-normal injection ($\beta = 90^o$) for $\hat{m} = 0.73$, $\hat{p} = -0.82$, and $\hat{q} = 0.79$; the markers represent Delta (△), Transition (◇), and Lambda (▽) cavities; Filled markers represent data from Barge model I, with δ_1, and empty markers represent data from Barge model II, δ_2; and the size of the marker represents the orifice size, *e.g.* (▵) $D_i \sim 5$ mm, (△) $D_i \sim 10$ mm, (△) $D_i \sim 20$ mm.

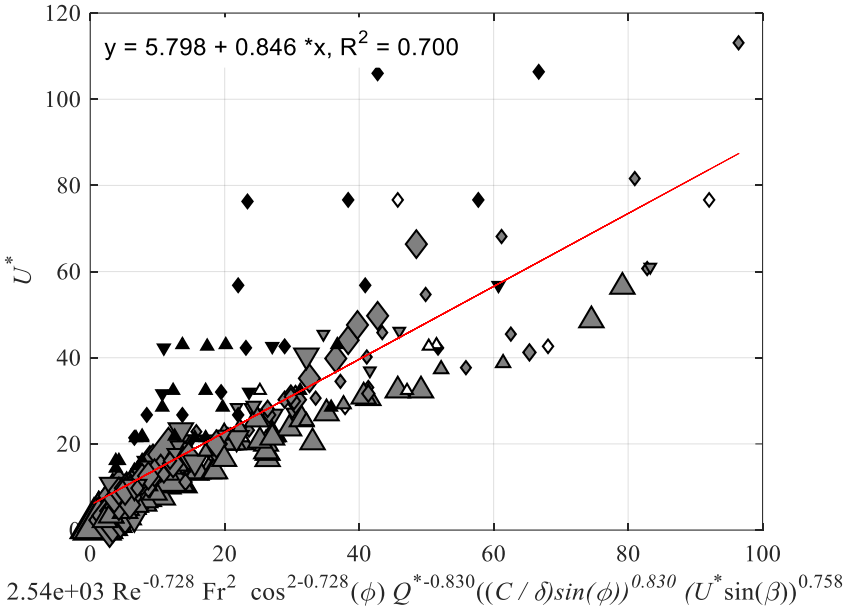

(a)

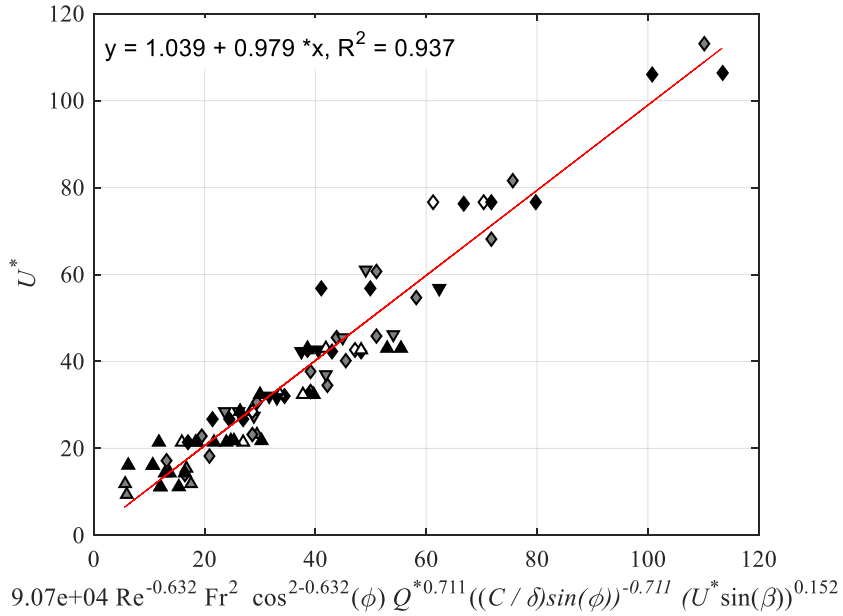

(b)

Figure 37: Same as figure 36 with additional data for angles injection. a) All hole diameters (angles ≠ 90° included only when D_i = 5mm) and b) only D_i = 5mm. For wall-normal injection (β = 90°, grey filled symbols), downstream injection (β < 90°, black filled symbols), and upstream injection (β > 90°, empty symbols); the markers represent Delta (△), Transition (◇), and Lambda (▽) cavities; the size of the marker represents the orifice size, *e.g.* (▵) D_i ~ 5 mm, (△) D_i ~ 10 mm, (△) D_i ~ 20 mm.

(a) (b) (c)

Figure 38: The modified orifice for wall-normal injection that includes a solid barrier (the half of a pipe extending beyond the pipe with larger outer diameter) upstream of the gas port (a); images of the cavity with D_i ~10 mm with U_∞ = 2.0 ms^{-1}, Q_i = 2.1x10^{-3} m^{3}s^{-1}, and $\delta \cong$ 19 mm for (b) the cavity topology resulting from injection with the plain orifice, and (c) the cavity topology resulting from placement of the barrier upstream on the injection port.

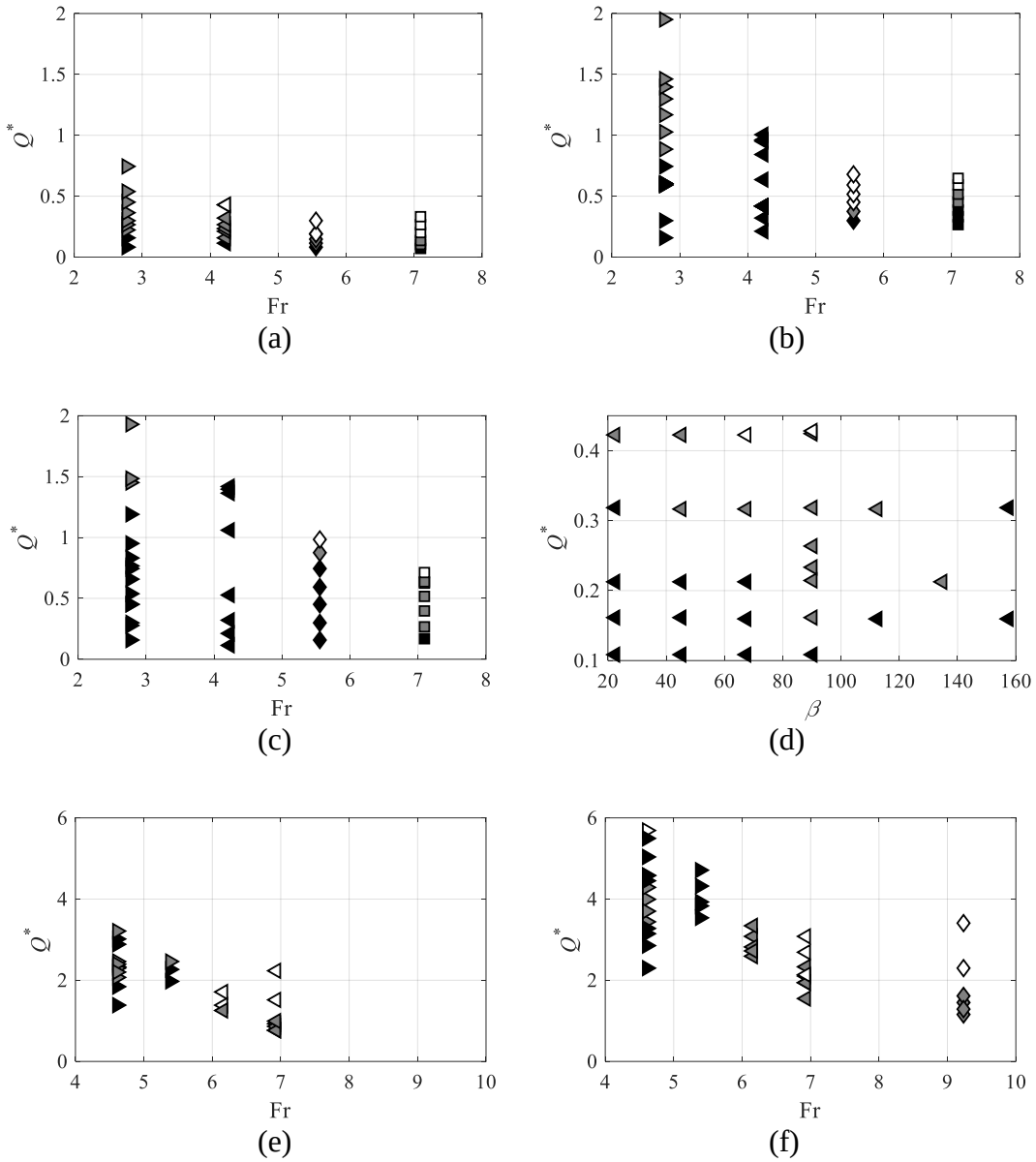

Figure 39: A map of the cavity topology boundaries as a function of Q^* *versus* Fr for β = 90° and for D_i = 5 mm (a), 10 mm (b), and 20 mm (c) with $\delta \cong 52$ mm. Topology map for Q^* *versus* β with D_i = 5 mm and Fr = 4.2. Topology map Q^* *versus* Fr for β = 90° and for D_i = 6 mm (e), and 10 mm (f) with $\delta \cong 17$ mm. The open symbols signify Lambda, grey Transitional and black filled a Delta-topology.

Parameter	Range	Uncertainty	Note
U_∞	1.0 $ms^{-1} < U_\infty <$ 5.0 ms^{-1}	$\pm$0.4%	The cross-flow equal to the carriage speed.
δ	15.8 mm $\leq \delta_1 \leq$ 19.1 mm 50.7 mm $\leq \delta_2 \leq$ 57.4 mm	δ_1 $\pm$1.0 mm δ_2 $\pm$2.8 mm	Boundary layer thicknesses on Barge I and Barge II.
D_i	Barge I: 6.0 mm and 10.0 mm Barge II: 4.9 mm, 10.2 mm, 19.7 mm	$\pm$0.1 mm	Nominal inner diameters are taken to be 5, 10, and 20 mm.
β	D_i = 5.0°; β = 22.5°, 45.0°, 67.5°, 90.0°, 112.5°, 135.0°, and 157.5°	$\pm$2°	When $\beta \neq$90, D_i is the diameter of the pipe leading to the orifice.
Q_i	1.0 x$10^{-4} \leq Q_i \leq$1.2 x10^{-2} m^3s^{-1}	<$\pm$10% of reading	Volume flow rate at draft pressure.
P_∞	102.1 kPa	$\pm$0.1 kPa	Static pressure draft pressure.

Table 1: Ranges and uncertainties of the parameters examined during the present study.

Mesh	Cells	Cell Size
Fine	11,836,364	2.0 mm
Medium	6,669,560	2.4 mm
Coarse	3,786,834	2.9 mm

Table 2: Parameters of the grid refinement study.

Case	U_∞ (ms^{-1})	Q_i (m^3s^{-1})	δ (mm)	φ (degrees)	C (mm)	e (mm)	St	***Type***	**Note**
A0	3	5.0 x10^{-3}	51	75.0 ±0.5		18.9	0.28	Λ	Coarse Grid
A1	3	5.0 x10^{-3}	51 (51.3)	76.5 ±0.5 (77.5±1.5)	97 (115±10)	19.4	0.29	Λ (Δ)	
A2	3	5.0 x10^{-3}	51	N/A	N/A	51	0.30		No Gravity
B	2	5.0 x10^{-3}	51 (52.8)	72.5 ±0.5 (70.4±1.5)	124 (124±5)	18.1	0.29	Λ (T)	
C	4	5.0 x10^{-3}	51 (53)	83.0 ±0.5 (84.9±1.5)	84 (66±5)	15.8	0.26	Λ (Λ)	
D	3	1.7 x10^{-3}	51 (51.3)	82.0 ±0.5 (84.7±1.5)	87 (N/A)	8.2	0.26	Δ (Δ)	Lower Gas Flux
E	3	5.0 x10^{-3}	17	80.5 ±0.5	79	17.0	0.30	Λ	1/3δ

Table 3: Conditions for the computed flows with the resulting sweep angle, chord length, and flow topology. The experimentally observed values are given below in parenthesis, along with the computed and observed cavity type (Δ, Λ, T). For all these cases, D_i ~ 10 mm and $\beta = 90^o$.

Parameter	Range	Note
Fr	$1.3 < \mathrm{Fr} < 7.2$	$\mathrm{Fr} = \frac{U_\infty}{\sqrt{g\delta}}$
Q^*	$6.7 \times 10^{-2} < Q^* < 1.4 \times 10^{1}$	$Q^* = \frac{Q_i}{U_\infty \delta^2}$
$\frac{D_i}{\delta}$	$7 \times 10^{-2} < \frac{D_i}{\delta} < 7 \times 10^{-1}$	
β	$22.5 < \beta < 157.5$ degreed	
$\frac{\rho_i}{\rho_\infty}$	1.2×10^{-3}	$\rho_i = 1.2$ kg m^{-3} $\rho_\infty = 1000$ kg m^{-3}
Π	$1.0 \times 10^{-3} < \Pi < 6.1 \times 10^{3}$	$\Pi = \frac{\rho_i {U_i}^2}{\rho_\infty {U_\infty}^2}$
Re_{D_i}	$3.6 \times 10^{3} < \mathrm{Re}_{D_i} < 1.0 \times 10^{5}$	$\mathrm{Re}_{D_i} = \frac{U_i D_i}{\nu_i}$
Re_δ	$1.5 \times 10^{4} < \mathrm{Re}_\delta < 2.9 \times 10^{5}$	$\mathrm{Re}_\delta = \frac{U_\infty \delta}{\nu_\infty}$

Table 4: Ranges of non-dimensional parameters of the present study.